Magnetic electron scattering and valence nucleon radial wave functions

S. K. Platchkov, J. B. Bellicard, J. M. Cavedon, B. Frois, D. Goutte, M. Huet, P. Leconte, and Phan Xuan-Ho
Département de Physique Nucléaire Centre d'Etudes Nucléaires de Saclay, 91191 Gif-sur-Yvette Cedex, France

P. K. A. de Witt Huberts and L. Lapikás
Nationaal Instituut voor Kernfysica en Hoge-Energiefysica, 1009 AJ Amsterdam, The Netherlands

I. Sick
Department of Physics, University of Basel, 4056 Basel, Switzerland
(Received 30 September 1981)

Cross sections have been measured for elastic electron scattering from the magnetization distributions of ^{49}Ti, ^{51}V, ^{59}Co, ^{87}Sr, ^{93}Nb, and ^{208}Bi. Particular emphasis has been placed on the multipole distribution of the highest order possible, which dominates the magnetic form factor at momentum transfer values q between 1.7 and 3.0 fm^{-1}. The data for the $1f_{7/2}$ shell nuclei ^{49}Ti, ^{51}V and for the $1g_{9/2}$ shell nuclei ^{87}Sr, ^{93}Nb are interpreted in terms of occupation probability and radial extension of the odd proton or neutron wave function. An accuracy of 1% is obtained for the valence orbit rms radii for both protons and neutrons. Corrections due to two-body magnetization currents and core polarization effects are investigated and found to be small. A detailed comparison of the experimental results with different types of density-dependent Hartree-Fock calculations is made in both momentum space and configuration space. It is found that the best available theory predicts the rms valence radii to within 2%. Comparisons are made between the present results and information on radial wave functions obtained from isotone shifts, proton scattering, and transfer reactions.

NUCLEAR REACTIONS ^{49}Ti, ^{51}V, ^{59}Co, ^{87}Sr, ^{93}Nb, ^{209}Bi(e,e); $E_0=175-325$ MeV, $\theta=155°$; $E_0=500$ MeV, $\theta=39-73°$; measured $\sigma(E_0,\theta)$; deduced magnetization distribution parameters, rms radii of neutron and proton $1f_{7/2}$ and $1g_{9/2}$ orbits.

I. INTRODUCTION

Elastic electron scattering at high momentum transfer brings out the fine details of the charge and magnetization densities of the nucleus in its ground state. The charge distribution of the nucleus is now known to such an accuracy that the experimental uncertainty is negligible, even in the interior region of the nucleus. Because of this high accuracy these experiments have provided an important testing ground for many-body theories attempting to describe the nuclear ground state. The determination of the magnetization distribution has been much more difficult, since the experimental data obtained for a large range of momentum transfer are usually an incoherent sum over all allowed multipoles. The interpretation of such data is difficult, and moreover quite sensitive to configuration mixing.

In the present paper we concentrate on one particular aspect of electron scattering: elastic magnetic scattering from the highest order multipole moment distribution. This highest magnetic multipole can be isolated experimentally on the high momentum transfer region, and can be interpreted[1] in terms of the radial wave function of the valence nucleon, with negligible uncertainty due to configuration mixing. Both the neutron and proton radial wave functions can be determined, a possibility which is of particular interest since neutron densities are usually derived from experiments with hadronic probes. The interpretation of hadronic experiments is subject to uncertainties in the reaction mechanism. Another major feature of electron

scattering from the highest magnetic multipole is its sensitivity to the inner region of the valence wave function. From such data we are able to determine the root mean square (rms) radii of the valence orbits studied with 1% accuracy for both protons and neutrons.

Several experimental methods have been used in the past for the determination of radial wave functions of individual shells. The difference between the charge densities of isotone pairs as determined by electron scattering yields information on the radial wave function $R(r)$ of the added proton. However, in order to extract $R(r)$, the core polarization effect caused by this proton must be known. This core polarization effect is usually estimated from a calculation and subtracted. The precision of the rms radius of the valence orbit obtained using this technique is at best $\pm 5\%$.

The momentum distribution of protons can be mapped out by knockout reactions such as $(p,2p)$ or $(e,e'p)$. These reactions are sensitive to the entire radial region and also permit the investigation of the deeply bound shells. Distortion effects, due to the final state interaction of the knocked out hadrons, limit the accuracy of the information obtained for the corresponding wave function. For $(e,e'p)$ reactions this distortion is less important, but the very low coincidence cross sections do not allow a measurement of the momentum distribution more precise than $\pm 3\%$.

Single nucleon transfer reactions may also be used to measure the wave function of the transferred nucleon, proton, or neutron. In transfer reactions the composite projectile is strongly absorbed, so these methods are primarily sensitive to the tail region of the wave function. This explains why the size of the nucleon orbit can be inferred only with large uncertainties, usually several percent.

In contrast, the magnetic elastic electron scattering experiments described in this paper are quite sensitive to the shape of the proton and neutron valence wave function throughout the nuclear volume. In the past, most magnetic elastic electron scattering experiments have been limited to low momentum transfer q (Ref. 2). The feasibility of mapping out the highest multipole of the magnetization density was demonstrated by Li *et al.*[3] for the $M9$ form factor of ^{209}Bi. The theoretical analysis for such experiments was developed by Donnelly and Walecka.[1] They showed that for odd-even nuclei with a stretched configuration and the maximum angular momentum of all occupied shells, the magnetic form factor at high momentum transfer is almost entirely due to the intrinsic magnetization density of the unpaired nucleon. In order to determine accurately the radial part of the valence wave function, the entire shape of the highest magnetic multipole must be known. It is therefore necessary to measure very small cross sections, down to 10^{-10} mb/sr. Such measurements have become possible only with the development of high intensity electron accelerators and a new generation of spectrometers and detectors.

In this paper we describe measurements for elastic electron scattering from the highest order magnetic multipoles of ^{49}Ti, ^{51}V, ^{59}Co, ^{87}Sr, ^{93}Nb, and ^{209}Bi. We have published partial accounts of these experiments in Refs. 4–7. In Sec. II we recapitulate briefly the theoretical framework needed to interpret magnetic form factors. In Secs. III and IV we describe the experimental setup and the data reduction procedures. The interpretation of the data in terms of radial wave functions is presented in Sec. V, while various corrections to this approach are discussed in Sec. VI. Section VII compares the experimental results to the predictions of self-consistent field theories. A comparison between the present results and information on valence wave functions obtained by other experimental techniques is presented in Sec. VIII. Our summary and conclusions are presented in the last section.

II. THEORETICAL FRAMEWORK

In this section we discuss electron scattering in terms of plane wave Born approximation (PWBA) and one-body operators. Distorted wave Born approximation (DWBA) and meson exchange currents will be considered in later sections.

The cross section for elastic scattering of electrons with incident energy E_0 can be written as:

$$\frac{d\sigma}{d\Omega}(E_0,\theta)=\left[\frac{d\sigma}{d\Omega}\right]_{\text{Mott}}\eta^{-1}\times[F_L{}^2(q)+(\tfrac{1}{2})\tan^2\tfrac{1}{2}\theta F_T{}^2(q)]\ . \quad (2.1)$$

In this expression $(d\sigma/d\Omega)_{\text{Mott}}$ is equal to $[(\alpha\cos\frac{1}{2}\theta)/2E_0\sin^2\frac{1}{2}\theta]^2$, θ is the scattering angle, and η is the recoil factor $1+(2E_0/M_T)\sin^2\frac{1}{2}\theta$ with M_T being the target mass. The longitudinal and the transverse form factors $F_L{}^2(q)$ and $F_L{}^2(q)$ are functions of the momentum transfer

$q=(2E/\eta^{1/2})\sin\frac{1}{2}\theta$.

The separation of transverse and longitudinal form factors can be performed with an appropriate combination of data taken at far backward and forward scattering angles at the same momentum transfer. In elastic scattering the transverse form factor is exclusively of magnetic character.

The magnetic form factor $F_T(q)$ is generated by the current and magnetization density distribution $\vec{j}(\vec{r})$ of the nuclear ground state. The density $\vec{j}(\vec{r})$ is given by the ground state expectation value of the nuclear current operator $\langle\psi_A|\hat{\vec{j}}(\vec{r})|\psi_A\rangle$, where

$$\hat{\vec{j}}(\vec{r})=\hat{\vec{j}}_c+\vec{\nabla}\times\hat{\vec{\mu}}(\vec{r}) . \tag{2.2}$$

Two terms contribute to the total current density operator: the convection current operator $\vec{j}_c(\vec{r})$ due to the protons and the intrinsic nucleon (proton *and* neutron) magnetization operator $\mu(\vec{r})$. (In principle, neutrons contribute to the orbital current at $q\neq 0$ as well, but their contribution may be neglected in this discussion.)

The squared form factor for scattering from a target with angular momentum J_0 can be written[1] as an incoherent sum over odd multipoles J:

$$F_T^2(q)=\sum_{J=1}^{2J_0}F_{MJ}^2(q)$$
$$=\frac{4\pi}{2J_0+1}\sum_{J=1}^{2J_0}|\langle\psi_A||\hat{T}_J^m(q)||\psi_A\rangle|^2 . \tag{2.3}$$

The many-body matrix element of the magnetic current operator $\hat{T}_J^m(q)$ can be expanded on a complete basis of orbital states:

$$\langle\psi_A||\hat{T}_J^m(q)||\psi_A\rangle=\sum_{\alpha,\beta}\rho_{\alpha\beta}^J\langle\alpha||\hat{T}_J^m(q)||\beta\rangle , \tag{2.4}$$

where $\rho_{\alpha\beta}^J$ is the one-body density matrix and the notation $\alpha=(n_\alpha, l_\alpha, j_\alpha, m_\alpha)$ is used for the quantum numbers specifying the state $|\alpha\rangle$. In the independent particle shell model (IPSM) with no residual interactions the current density is exclusively determined by the odd-nucleon wave function $|\alpha_0\rangle$, i.e., only $\rho_{\alpha_0\alpha_0}^J\neq 0$ in Eq. (2.4).

The interpretation of magnetic scattering data becomes particularly simple if the following conditions are satisfied: The valence nucleon has the highest J value of all occupied orbits, it is in a stretched configuration ($J_0=l+\frac{1}{2}$), and the highest allowed multipolarity is considered. These conditions lead to the following remarkable properties:

The highest magnetic multipole $F_{M\Lambda}$ largely dominates F_T in the range of momentum transfer $q=(1.8-3.0)$ fm^{-1} as illustrated in Fig. 1. $F_{M\Lambda}$ is then measurable with only minor interference from the lower multipole components. Since scattering of multipolarity $\Lambda=2J_0$ corresponds to a complete spin-flip of the nucleus, shells with J values $J<J_0$ cannot contribute. Moreover, the highest multipolarity receives no contribution from the convection current. Ignoring admixtures with $J>J_0$ one obtains:

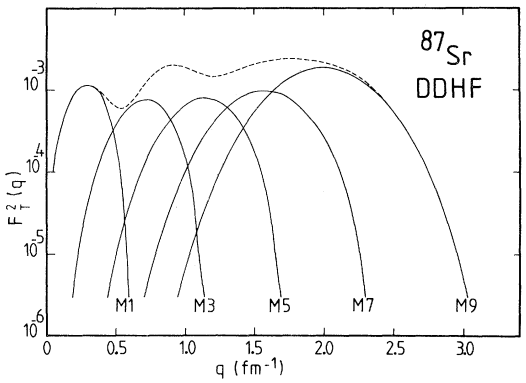

FIG. 1. Magnetic form factor for ^{87}Sr nucleus calculated in PWBA using a DDHF (Ref. 44) $1g_{9/2}$ neutron wave function. For clarity only the first maxima of each multipole (solid curves) are shown. The total form factor (dashed line) is also plotted.

$$F_{M\Lambda}(q)=\left[\frac{4\pi}{2J_0+1}\right]^{1/2}\rho_{\alpha_0\alpha_0}^{\Lambda}\langle\alpha_0||\hat{T}_\Lambda^m(q)||\alpha_0\rangle . \tag{2.5}$$

It follows that the q dependence of $F_{M\Lambda}$ is characteristic of $|\alpha_0\rangle$. It is related to the radial wave function $R_{\alpha_0}(r)$ by the following expression:

$$F_{M\Lambda}=C_\Lambda\alpha_\Lambda\mu\frac{q}{M}$$
$$\times\int_0^\infty R_{\alpha_0}(r)j_{\Lambda-1}(qr)r^2dr . \tag{2.6}$$

Here $j_{\Lambda-1}(qr)$ is the spherical Bessel function of order $\Lambda-1$, $M(\mu)$ is the nucleon mass (magnetic moment), α_Λ is the spectroscopic amplitude of the state, and C_Λ is a coefficient equal to $7\times5\times(13\times11\times7\times\frac{3}{2})^{1/2}$ or $3\times7\times(11\times13\times\frac{17}{5})^{-1/2}$ for F_{M7} or F_{M9}, respectively. In Fig. 2 we give $R^2(r)$ for a typical case, the $g_{9/2}$ neutron wave function of ^{87}Sr, together with the integrand of Eq. (2.6) for two typical values of q. Figure 2 shows that the experiment is mainly sensitive to the radial region where $R^2(r)$ is large, i.e., the region between 2 and 6

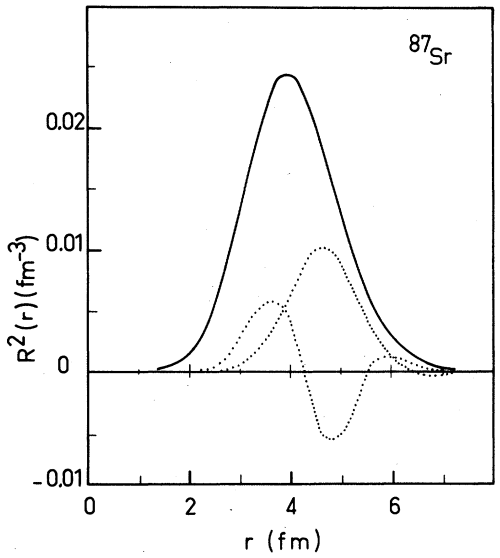

FIG. 2. $1g_{9/2}$ radial wave function squared for ^{87}Sr (solid line) shown together with the integrand [Eq. (2.6)] for momentum transfers of 2 and 3 fm^{-1} (dotted).

fm. The density at very large radius does not significantly influence $F_{M\Lambda}$.

The $1\hbar\omega$ excitations present in the ground state cannot couple to an angular momentum J_0 because of the parity conservation. In order to have additional single particle matrix elements contributing to $F_{M\Lambda}(q)$ one must admix (2p-2h) states with $\vec{j}_1+\vec{j}_2>\vec{J}_0$ into the ground state. These states are far removed in energy and have a small amplitude. Provided that the ground state has a fairly pure single particle configuration, we expect to be able to describe $F_{M\Lambda}(q)$ by simply scaling the single particle matrix element with a coefficient $\rho^{\Lambda}_{\alpha_0\alpha_0}$ representing the depletion due to the configuration admixtures with $\vec{j}_1+\vec{j}_2<\vec{J}_0$. For near spherical nuclei we shall show in Sec. VI A that the effect of such admixtures on $F_{M\Lambda}$ is negligible indeed.

These considerations show that for the case considered—maximum angular momentum, highest multipole order, stretched configuration—the interpretation is particularly simple. For our experiment we have chosen three $f_{7/2}$ shell nuclei (^{49}Ti, ^{51}V, ^{59}Co), two $g_{9/2}$ nuclei (^{87}Sr, ^{93}Nb), and an $h_{9/2}$ nucleus (^{209}Bi). Only ^{209}Bi and ^{59}Co do not satisfy the required conditions: ^{209}Bi has a jackknifed configuration ($J_0=l-\frac{1}{2}$), whereas ^{59}Co has a deformed ground state. We therefore expect that only the data for ^{49}Ti, ^{51}V, ^{87}Sr, and ^{93}Nb can be interpreted unambiguously in terms of individual nucleons valence densities. These nuclei will therefore receive special attention in our quantitative analysis.

III. DESCRIPTION OF THE EXPERIMENT

Cross sections for elastic electron scattering have been measured at the 600 MeV Accélérateur Linéaire de Saclay (ALS). The standard equipment

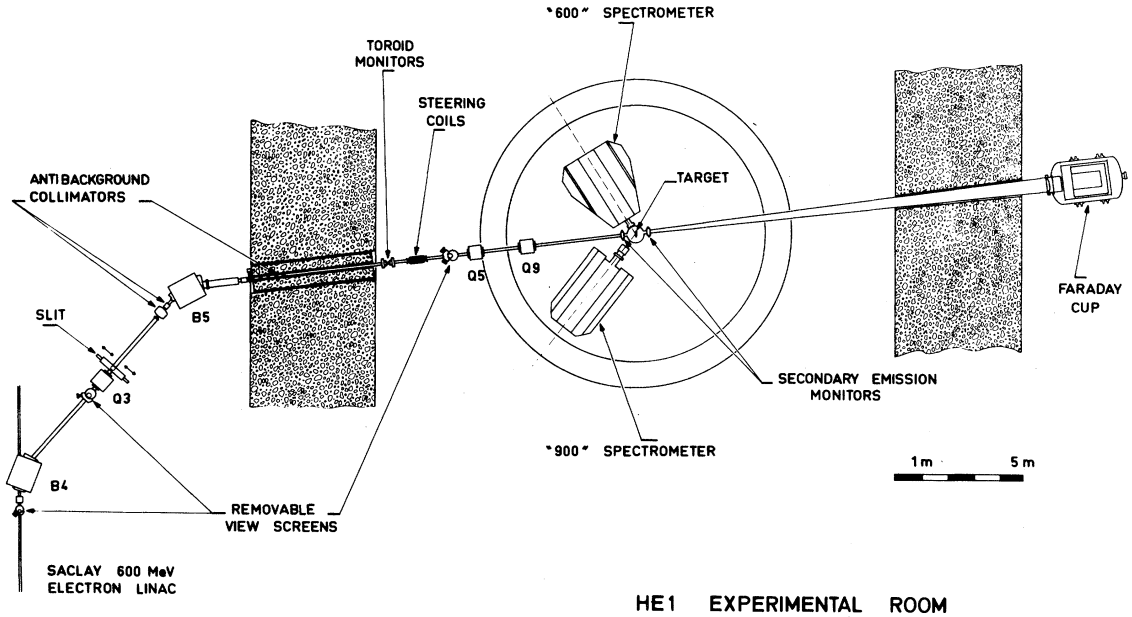

FIG. 3. Layout of the beam switchyard and the HE1 experimental hall.

of the HE1 end station has been used. The general features of the coincidence setup have been discussed in a previous publication.[8] We shall emphasize here the details of the single arm facility.

A. Beam

A simplified layout of the equipment is shown in Fig. 3. The electron beam with a one percent duty cycle and an average current of 100 μA is deflected by two 41° bending magnets. It is dispersed by the first magnet and hits the energy defining slit, the dispersion of which is 0.3 mm for $\Delta p/p = 10^{-4}$. For the momentum spread of 5×10^{-4} used for this experiment, it has a transmission factor of 0.15. The shower created by the slit is eliminated by collimators and absorbers placed along the beam line. The second magnet and a quadrupole are used to obtain a completely achromatic system.

A precise alignment of the beam is obtained using four steering coils and two viewers which can intercept the beam simultaneously. A pair of quadrupoles are used to focus the beam at the center of the target. The beam halo is reduced to a minimum: Only 1% of the electrons were found to be outside of a 0.7×2 mm^2 rectangle at the target position.

The total beam charge is measured by means of ferrite toroid monitors and a Faraday cup. The Faraday cup is water cooled in order to be able to dissipate the high power (maximum $\sim$100 kW) deposited by the incoming beam. To avoid backscattered electrons and neutron background, it is located in a separate hall at a 15 m distance from the center of the target. To keep multiple scattering losses low it was built with a 60 cm aperture. The multiple scattering loss—of the order of few percent—was measured at different energies for a series of nuclei, and parametrized by the quantity $1/E_0\sqrt{t/x_0}$, where t is the effective target thickness and x_0 the radiation length of the material. Owing to ionization of the water by the beam induced radiation, some off-set current I_R could be present. This current (typically 10–20 nA) was periodically measured, and compensated by injecting $-I_R$.

The ferrite toroid monitors are positioned upstream of the scattering chamber. The induced signal is gated and integrated, providing a measurement proportional to the charge of the beam passed through the monitors. The obtained value is compared to a calibrated charge pulse injected between two consecutive beam pulses. The incident beam and the test pulse are measured with the same electronics, thus eliminating systematic errors. The accuracy of this system is 1% for average currents of more than 1 μA. In all measurements both the Faraday cup and the ferrite monitors were used. The precision thus obtained on the collected charge is better than 1%.

B. Targets

Up to 12 solid targets can be accommodated on a wheel placed in the 50 cm scattering chamber. For most of the targets the main problem was the dissipation of the deposited beam power. This is done by:

(a) moving the wheel in the target plane following a Lissajous pattern; the beam is thus spread over an area of typically 15×10 mm^2;

(b) cooling both sides of the target by a jet of hydrogen gas ($\sim$1 Torr); 0.5 W/cm^2 are dissipated in such a way for 600 K target temperature; and

(c) defocusing the beam spot in order to reduce the instantaneous power density on the target.

Combined use of these precautions allowed us to use average currents from 10 to 20 μA without melting the targets. Such intensities are necessary to measure the extremely small cross sections ($\sim10^{-37}$ cm^2/sr) occurring at the higher momentum transfers.

The properties of the targets used are summarized in Table I. The isotopic purities are known with a precision better than 0.2%. The target thickness was determined from the weight and area

TABLE I. Targets used in the experiment. Isotopic purities were given by the manufacturer, Oak Ridge National Laboratory (ORNL).

Nucleus	Isotopic purity (%)	Thickness (mg/cm^2)
$^{49}_{22}$Ti^{27}	81.6	98.4
$^{51}_{23}$V^{28}	99.8	79.0
$^{59}_{27}$Co^{32}	100.0	110.7
$^{87}_{38}$Sr^{49}	93.3	98.5
$^{93}_{41}$Nb^{52}	100.0	94.0
$^{209}_{83}$Bi^{126}	100.0	124.0;251.0
$^{48}_{22}$Ti^{26}	99.3	97.5
$^{88}_{38}$Sr^{50}	99.8	96.0
$^{208}_{82}$Pb^{126}	99.2	97.0;110.0

method. This gives an accuracy of 2–3 % depending on the target homogeneity. A ^{12}C target with a well known (1%) thickness was used for the absolute calibration runs. To keep the energy spread as low as possible, the target angle was always fixed to half the scattering angle in transmission mode. The target angles are known with an accuracy of 0.1 deg, yielding a maximum error of 0.8% on the effective target thickness for scattering at the most backward angle $\theta=155°$.

C. Spectrometer

Scattered electrons are analyzed in a double focusing magnetic spectrometer[9] (Fig. 4) called "900" according to the maximum momentum (MeV/c) of the analyzed particles. It is built for high resolution and low cross section experiments. It is derived from the "magic angle" spectrometer ($\theta=169.7$, $n=0.5$, $\beta=0.25$), with vanishing second order aberrations. This design was modified in order to obtain a small transverse dimension (<20 mm) of the image in the focal plane. The actual β is 1.6 and curved poles are used. The resulting angle between electron trajectory and focal plane is 39°.

The momentum acceptance of the spectrometer is 10%. For magnetic fields up to 1.1 T its intrinsic resolution remains the same: It varies from 1×10^{-4} to 2×10^{-4} along the focal plane for the maximum solid angle. The magnetic field is measured by a nuclear magnetic resonance (NMR) probe. In combination with the precisely known fields maps this yields an absolute energy calibration with an accuracy better than 10^{-4}.

The dispersion along the focal plane is 1 mm for $\delta p/p=0.9\times10^{-4}$. The focal plane is a slightly curved surface with 3 cm deviation from a plane over its 1 m total length. The detector has been designed to fit this curvature. The spectrometer can be rotated from 25 to 155 deg. It has eight collimators, defining solid angles ranging from 0.017 to 4.85 msr, and known with 0.5% accuracy. The largest solid angles ($\Delta\Omega=3$ and 4.85 msr) were used for the low cross section data. Measurements with higher counting rates were made using smaller collimators ($\Delta\Omega=0.113$ and 0.46 msr).

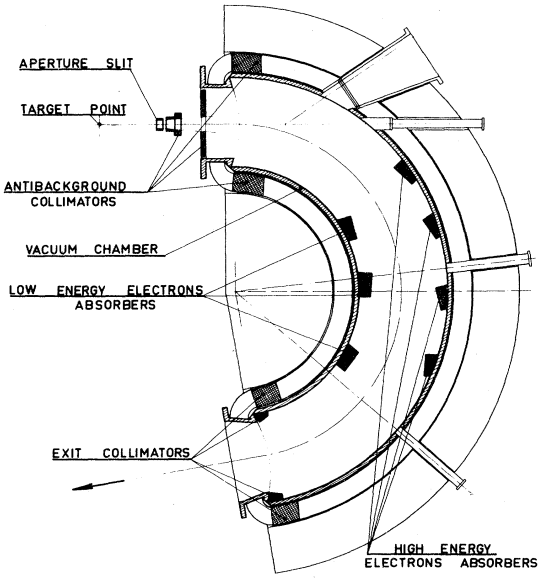

FIG. 4. The 900 MeV/c magnetic spectrometer.

D. Detectors and background rejection

The detection system (Fig. 5) was built according to the following criteria: to detect the scattered particles with good energy resolution; to be able to measure cross sections with a dynamic range of at least eight decades, with constant efficiency and minimum dead time; and to have the best possible background rejection. This is an important condition for measurements of very low cross sections.

The detection system consists of two sets of plastic scintillators (R and Y), a Čerenkov counter (C), and two multiwire proportional counters (MWPC).[10] The first MWPC (E) is placed in the focal plane. It has 512 wires, defining 1024 channels. The wires are 2 mm apart and perpendicular to the symmetry plane of the spectrometer. The second MWPC (X) has 640 wires and defines 160 channels. Both wire chambers are filled with 88% argon and 12% ethylbromide. The average cluster size of the hit wires per event is three. The particle

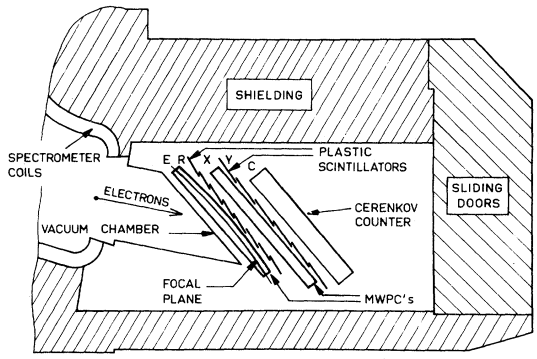

FIG. 5. The detection system of the 900 spectrometer. E and X: multiwire proportional counters; R and Y: scintillators planes; C, Čerenkov counter.

trajectory is calculated from the center of gravity of the touched wires. The energy resolution of the E chamber is 2×10^{-4}.

A threefold fast coincidence between the R, Y, and C planes defines the trigger for readout of the E and X counters. For each chamber the only scanned areas are those corresponding to the R_i scintillators touched. The X chamber measures the angle of the scattered electrons relative to the optical axis of the spectrometer. Computer software accepts only electrons following normal trajectories coming from the target through the spectrometer. About 10% of the observed electrons are rejected by this criterion. The lowest cross section measured in this experiment was 2.17×10^{-37} cm^2/sr, which corresponds to three counts in the elastic peak without any background.

E. Data acquisition

The electronics used with the MWPC is described in detail in Ref. 11. It was designed to accept up to two events per beam burst for a large number of detecting channels. The associated logic creates eight 16-bits words for each event. Up to 128 events can be stored in a buffer memory, before being transferred to the PDP 15/30 data acquisition computer. At the end of the run all the relevant parameters together with the experimental spectra are saved on magnetic tape. Elastic cross sections are calculated on-line, thus allowing rapid quantitative evaluation of the experimental results.

IV. DATA REDUCTION AND EXPERIMENTAL RESULTS

A. Experimental procedure

In order to isolate the magnetic scattering cross section the experiments have been performed in two steps:

(1) The charge scattering has been determined at forward angles and high incident energy. Angular distributions were measured at 500 MeV between 1.7 and 3 fm^{-1} for all the nuclei studied. At this energy the cross sections are mainly longitudinal with a small magnetic scattering contribution.

(2) Cross sections for same nuclei were then measured at an angle of 155°, where the magnetic contribution is dominant. The incident energies E_0 for which significant measurements can be performed were in the range from 175 to 325 MeV. For E_0 lower than 175 MeV the cross sections begin to be dominated by charge scattering. At energies higher than 325 MeV the counting rate would have been lower than one count per day.

In the case of nuclei with an unpaired neutron (^{49}Ti and ^{87}Sr) the cross sections of the nearest even-even isotope (^{48}Ti and ^{88}Sr) were also measured under identical experimental conditions. By taking the cross section differences at 155° and ratios at 500 MeV and forward angles, systematic uncertainties in the charge contribution subtraction are minimized; the final magnetic form factors are thus derived with better accuracy.

At each energy, normalization runs using a carbon target were also made. The carbon cross sections were always measured at identical values of momentum transfer ($q=1.0$ to 1.1 fm^{-1}) for each incident energy. The measurements were done before and after the 155° runs in order to monitor the overall stability in the experimental equipment. Quasielastic spectra of carbon were also taken in

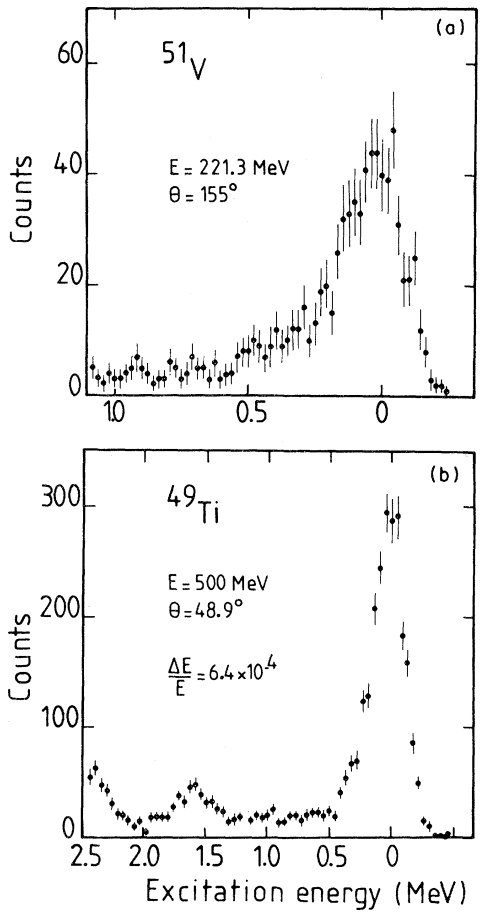

FIG. 6. Typical experimental spectra at forward (a) and backward (b) scattering angles.

order to determine the relative efficiency of individual detector channels.

At forward scattering angles the resolution $\Delta E/E$ was mainly limited by the energy spread of the incident beam. Typical values of $\Delta E/E$ were 5×10^{-4} to 10^{-3}. At 155° the effective target thickness becomes large ($t_{\text{eff}}=4.6t$ for transmission mode). In this case Landau straggling becomes the largest contribution to $\Delta E/E$, giving rise to a resolution of the order of 1×10^{-3}. For the nuclei of interest this is sufficient to resolve the elastic peak from the first excited state.

Typical examples of the experimental spectra are shown in Fig. 6. No background was observed at energies above the elastic peak. It was therefore possible to measure cross sections as low as 10^{-37} cm^2/sr (a few counts per day) without any ambiguity.

B. Data reduction

The total number of elastically scattered electrons was obtained by correcting the experimental spectra for the radiative effects. The different terms contributing to the radiative corrections are discussed in detail by Mo and Tsai.[12] Two different approaches were used for the calculation of the differential cross sections:

(a) The area of the experimental elastic peak is integrated up to a cutoff ΔE_c and then corrected for the integrated probability to find elastically scattered electrons beyond ΔE_c. A value of $\Delta E_c=0.7$ MeV was used for all nuclei except ^{87}Sr for which a value of $\Delta E_c=0.63$ MeV was chosen. Such a cutoff integrating the peak beyond $\Delta E_c=0.7$ MeV leaves the cross section constant within 1%.

(b) The second method has been described in detail by Crannell.[13] The experimental electron spectrum is divided into consecutive, equal energy bins of $dE/E=10^{-4}$. Starting from the higher energy end of the spectrum, the radiative tails of consecutive bins are calculated and unfolded. Both methods give the same result to 1% for runs with a

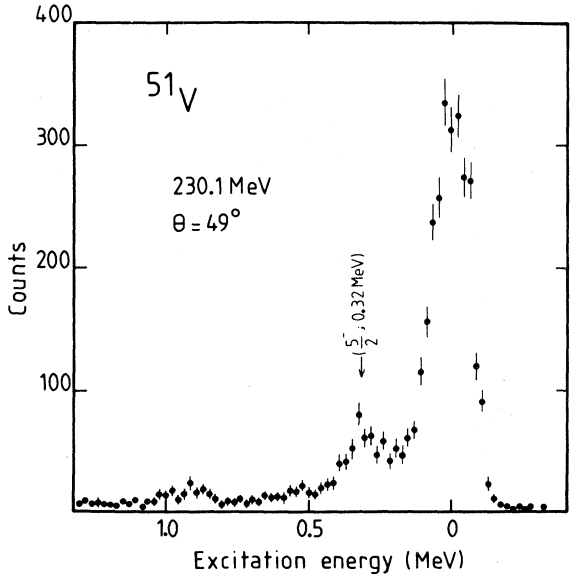

FIG. 7. Contribution of the ^{51}V $\frac{5}{2}^-$ excited state to the experimental spectrum.

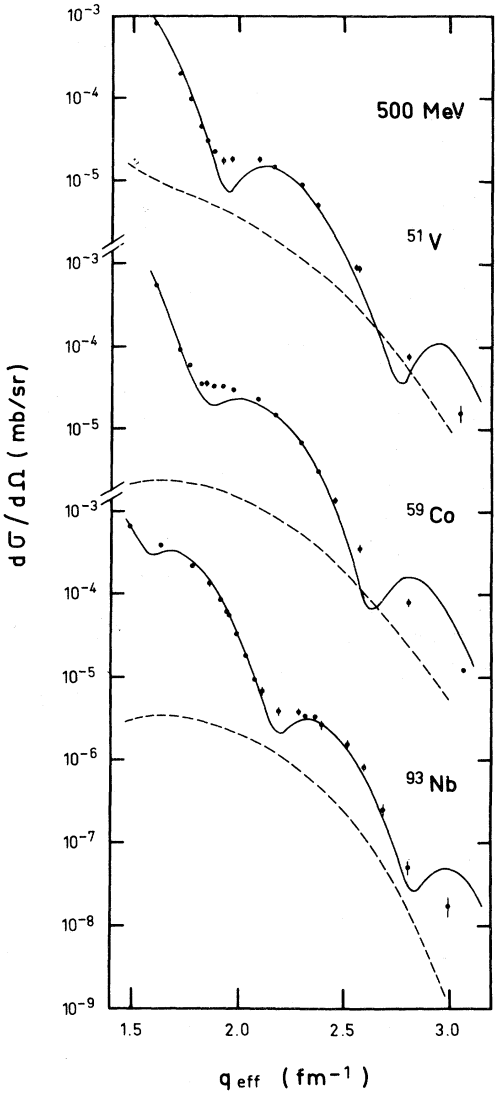

FIG. 8. Forward angle cross sections for ^{51}V, ^{59}Co, and ^{93}Nb nuclei. The fit to the data (solid line) and the magnetic contribution (dashed line) calculated from the backward angle data are also shown.

TABLE II. Total and magnetic cross sections at 155° and transverse form factor for ^{49}Ti nucleus.

E_0 (MeV)	q_{eff} (fm^{-1})	$(d\sigma/d\Omega)_{\text{tot}}$ (mb/sr)	$(d\sigma/d\Omega)_m$ (mb/sr)	$F_T{}^2$
175.2	1.800	$5.11(18)\times10^{-7}$	$3.68(24)\times10^{-7}$	$2.04(13)\times10^{-3}$
175.2	1.800	$4.55(33)\times10^{-7}$	$3.73(46)\times10^{-7}$	$2.07(25)\times10^{-3}$
191.0	1.959	$3.66(14)\times10^{-7}$	$2.96(20)\times10^{-7}$	$1.95(13)\times10^{-3}$
191.0	1.959	$3.36(28)\times10^{-7}$	$2.71(41)\times10^{-7}$	$1.79(27)\times10^{-3}$
205.7	2.107	$3.40(14)\times10^{-7}$	$1.91(20)\times10^{-7}$	$1.46(15)\times10^{-3}$
205.7	2.107	$3.00(27)\times10^{-7}$	$1.78(42)\times10^{-7}$	$1.37(32)\times10^{-3}$
220.1	2.251	$2.44(10)\times10^{-7}$	$1.68(14)\times10^{-7}$	$1.47(13)\times10^{-3}$
235.1	2.402	$1.32(7)\times10^{-7}$	$1.09(10)\times10^{-7}$	$1.10(10)\times10^{-3}$
250.0	2.551	$5.66(40)\times10^{-8}$	$5.91(57)\times10^{-8}$	$6.70(64)\times10^{-4}$
275.1	2.802	$1.16(9)\times10^{-8}$	$1.39(14)\times10^{-8}$	$1.90(19)\times10^{-4}$
300.0	3.051	$1.81(28)\times10^{-9}$	$2.11(32)\times10^{-9}$	$3.45(52)\times10^{-5}$
325.1	3.300	$2.17(83)\times10^{-10}$	$1.93(12)\times10^{-10}$	$3.71(2.36)\times10^{-6}$

high number of events per channel. For low counting rates (small number of events in the elastic peak) the cutoff method is preferred.

The first excited state of ^{51}V is at 0.32 MeV and must be resolved from the elastic peak. At forward scattering angles and low energies we found its contribution to be less than 5% of the area of the elastic peak (Fig. 7). For the final forward angle data the contribution of that $\frac{5}{2}^-$ level was subtracted. Owing to the weak excitation of this level the resulting uncertainty is unimportant. At backward scattering angles the contribution of this low multipolarity excitation, as calculated in shell model framework, is negligible; indeed at 175.2 MeV no excited level contamination was observed both in reflection and transmission target geometry.

An *a priori* contribution of the first excited level of ^{87}Sr (0.39 MeV) would also be possible. This is a metastable level with a lifetime of 2.83 h and with a spin assignment of $\frac{1}{2}^-$. Single particle model estimates indicate that the inelastic $M4$ and $E5$ strengths are negligible in our momentum transfer range. We would see no evidence for a contribution from this level in any of our experimental spectra.

Given the uncertainties discussed above, a 3% systematic error was ascribed to all our measurements. When cross section ratios were used, only statistical errors were taken into account.

The ^{12}C elastic cross sections were compared to the best fit of Sick and McCarthy.[14] The ratio of the fit to the measured value was defined as a normalization factor. For all measurements we found this normalization factor to be close to 1.10. At each energy no fewer than three data points have been measured; the values obtained yield the same normalization factor which, over the period of several years, fluctuated by $\sim$5%. Dead time corrections have been applied to the high counting

TABLE III. Same as Table II but for ^{51}V.

E_0 (MeV)	q_{eff} (fm^{-1})	$(d\sigma/d\Omega)_{\text{tot}}$ (mb/sr)	$(d\sigma/d\Omega)_m$ (mb/sr)	$F_T{}^2$
176.2	1.814	$1.43(10)\times10^{-6}$	$1.31(10)\times10^{-6}$	$7.28(55)\times10^{-3}$
191.0	1.963	$1.15(6)\times10^{-6}$	$9.46(60)\times10^{-7}$	$6.19(40)\times10^{-3}$
205.0	2.103	$1.00(4)\times10^{-6}$	$8.08(35)\times10^{-7}$	$6.09(26)\times10^{-3}$
221.3	2.267	$5.67(52)\times10^{-7}$	$4.42(52)\times10^{-7}$	$3.88(46)\times10^{-3}$
230.1	2.355	$4.04(17)\times10^{-7}$	$3.30(17)\times10^{-7}$	$3.12(17)\times10^{-3}$
235.0	2.405	$3.17(17)\times10^{-7}$	$2.66(17)\times10^{-7}$	$2.63(17)\times10^{-3}$
251.3	2.568	$1.28(10)\times10^{-7}$	$1.21(10)\times10^{-7}$	$1.37(11)\times10^{-3}$
274.6	2.802	$3.00(20)\times10^{-8}$	$2.92(20)\times10^{-8}$	$3.91(27)\times10^{-4}$
300.0	3.056	$4.74(90)\times10^{-9}$	$4.50(90)\times10^{-9}$	$7.2(1.4)\times10^{-5}$

TABLE IV. Same as Table II but for ^{87}Sr.

E_0 (MeV)	q_{eff} (fm^{-1})	$(d\sigma/d\Omega)_{\text{tot}}$ (mb/sr)	$(d\sigma/d\Omega)_m$ (mb/sr)	$F_T{}^2$
191.2	1.995	$4.17(44)\times10^{-7}$	$1.84(48)\times10^{-7}$	$1.21(31)\times10^{-3}$
204.8	2.134	$2.01(22)\times10^{-7}$	$2.01(24)\times10^{-7}$	$1.51(18)\times10^{-3}$
214.1	2.229	$1.72(20)\times10^{-7}$	$1.66(21)\times10^{-7}$	$1.36(17)\times10^{-3}$
219.4	2.283	$1.45(17)\times10^{-7}$	$1.28(18)\times10^{-7}$	$1.10(15)\times10^{-3}$
235.0	2.443	$8.14(91)\times10^{-8}$	$5.89(99)\times10^{-8}$	$5.82(98)\times10^{-4}$
249.5	2.591	$3.86(47)\times10^{-8}$	$2.96(51)\times10^{-8}$	$3.31(57)\times10^{-4}$
274.6	2.846	$5.75(90)\times10^{-9}$	$6.11(97)\times10^{-9}$	$8.20(1.30)\times10^{-5}$
288.8	2.992	$2.50(50)\times10^{-9}$	$2.40(60)\times10^{-9}$	$3.60(90)\times10^{-5}$

rate data. This well known correction was always smaller than 5%.

C. Magnetic form factors

The general expression for the electron scattering cross section consists of a charge and magnetic part:

$$\left[\frac{d\sigma}{d\Omega}\right]_{\text{tot}} = \left[\frac{d\sigma}{d\Omega}\right]_{\text{ch}} + \left[\frac{d\sigma}{d\Omega}\right]_m .$$

We used two different methods to separate the magnetic contribution from the total cross section. In the case of the ^{51}V, ^{59}Co, and ^{93}Nb nuclei, we first assumed that the forward angle data are only due to pure charge scattering. These data (available on request) were fitted using a phase-shift code with three parameter Gaussian charge densities. The resulting fits together with the data points are shown in Fig. 8.

The best fit model densities were used to calculate the charge contribution at 155° via a phase shift code. Subtracting it from the experimental data we obtain a first estimate of the backward angle magnetic cross section. Assuming the validity of the q-effective transformation (Sec. V A) we then utilize the magnetic cross sections measured at 155° to obtain the magnetic part of the forward angle data at 500 MeV. These forward angle magnetic cross sections are then subtracted from the experimental data to obtain a better estimate of the charge scattering cross sections which are once again fitted with a three parameter Gaussian charge density. One more iteration of this process is sufficient to obtain a consistent set of magnetic and charge cross sections. The resulting magnetic cross sections are listed in Tables III, V, and VI. The magnetic form factors are obtained from Eq. (2.1).

An alternative method was used for ^{49}Ti and ^{87}Sr data for which the cross sections of the neighboring even-even isotopes were measured at the same angles and energies. Neglecting the forward angle magnetic scattering, the 155° magnetic cross section is given by the expression

$$\left[\frac{d\sigma}{d\Omega}\right]_m = \left[\left[\frac{d\sigma}{d\Omega}\right]_{\text{tot}} - \left[\frac{d\sigma}{d\Omega}\right]_{\text{ch}} r(500)\right]\frac{1}{\gamma} ,$$

where $r(500)$ is the 500 MeV ratio, e.g., ^{87}Sr/^{88}Sr at the same q_{eff} as the 155° measurements and γ is a correction for the isotopic purity of the targets employed. The ratio $r(500)$ contains a small magnetic

TABLE V. Same as Table II but for ^{93}Nb.

E_0 (MeV)	q_{eff} (fm^{-1})	$(d\sigma/d\Omega)_{\text{tot}}$ (mb/sr)	$(d\sigma/d\Omega)_m$ (mb/sr)	$F_T{}^2$
176.0	1.846	$1.94(12)\times10^{-6}$	$6.70(1.20)\times10^{-7}$	$3.72(65)\times10^{-3}$
191.0	1.999	$6.56(34)\times10^{-7}$	$5.09(34)\times10^{-7}$	$3.34(22)\times10^{-3}$
206.2	2.154	$4.28(23)\times10^{-7}$	$3.96(23)\times10^{-7}$	$3.03(17)\times10^{-3}$
221.3	2.310	$3.19(20)\times10^{-7}$	$2.64(20)\times10^{-7}$	$2.29(17)\times10^{-3}$
236.3	2.464	$1.56(9)\times10^{-7}$	$1.25(9)\times10^{-7}$	$1.25(9)\times10^{-3}$
251.3	2.617	$4.41(44)\times10^{-8}$	$3.91(44)\times10^{-8}$	$4.42(50)\times10^{-4}$
276.0	2.870	$3.70(1.1)\times10^{-9}$	$2.90(1.10)\times10^{-9}$	$3.94(1.5)\times10^{-5}$

TABLE VI. Same as Table II but for ^{59}Co.

E_0 (MeV)	q_{eff} (fm^{-1})	$(d\sigma/d\Omega)_{\text{tot}}$ (mb/sr)	$(d\sigma/d\Omega)_m$ (mb/sr)	$F_T{}^2$
176.2	1.821	$7.95(30)\times10^{-7}$	$4.45(46)\times10^{-7}$	$2.49(36)\times10^{-3}$
191.0	1.972	$7.07(35)\times10^{-7}$	$3.57(38)\times10^{-7}$	$2.34(33)\times10^{-3}$
206.2	2.126	$5.02(23)\times10^{-7}$	$2.87(25)\times10^{-7}$	$2.20(23)\times10^{-3}$
221.3	2.278	$2.84(16)\times10^{-7}$	$2.03(19)\times10^{-7}$	$1.79(23)\times10^{-3}$
236.2	2.429	$1.37(8)\times10^{-7}$	$1.26(10)\times10^{-7}$	$1.28(10)\times10^{-3}$
251.3	2.580	$6.45(60)\times10^{-8}$	$6.14(60)\times10^{-8}$	$6.99(70)\times10^{-4}$
275.1	2.829	$1.04(17)\times10^{-8}$	$9.70(18)\times10^{-9}$	$1.31(24)\times10^{-4}$
300.0	3.070	$1.30(30)\times10^{-9}$	$1.00(30)\times10^{-9}$	$1.62(48)\times10^{-5}$

contribution; it has been removed through use of the q-effective transformation. The obtained magnetic cross sections and form factors are summarized in Tables II and IV.

This last method was also applied to the ^{209}Bi data. The data of Sick[15] were used for the Bi/Pb forward angle ratio, while our backward angle data were used to obtain the magnetic contribution to this ratio. At incident energies of 176.3, 182, 191, and 203.7 MeV, the 155° cross sections for the ^{208}Pb nucleus were also measured and subtracted from the ^{209}Bi data. At higher energies the 155° lead cross sections are too small to measure easily, so we preferred to subtract the charge contribution by calculation, using the sum-of-Gaussian[16] fit to our recent experiment.[17] The resulting ^{209}Bi data are summarized in Table VII.

Except for ^{209}Bi our data cover the entire region of momentum transfer ($q=1.8$ to 3 fm^{-1}) where the $M\Lambda$ form factor can be separated reasonably well from the other multipoles. For lower values of q $M\lambda$ ($\lambda<\Lambda$) form factors dominate the transverse cross section, whereas at very large q one cannot disentangle $M\Lambda$ from the other multipoles. Magnetic form factors were previously measured at Sendai[18,19] for ^{51}V and ^{209}Bi nuclei; these data cover only the maximum region ($q_{\max}=2.3$ fm^{-1}) of the $M\Lambda$ multipole. Recently, data of good accuracy were taken at Bates[20] for ^{93}Nb. These data also extend to 2.2 fm and agree with our measurements in the medium q region.

V. DATA ANALYSIS AND FIT RESULTS

Our magnetic form factors will be compared to predictions of Hartree-Fock theory in Sec. VII. In order to allow for a comparison in r space as well, we first derive here phenomenological radial wave functions used to fit the data.

A. Radial wave function basis

Rather than parametrizing the radial wave function $R(r)$ of the valence nucleon (as done, e.g., for the charge density when analyzing charge scattering) we parametrize the effective local potential V in which the valence nucleon is bound. This procedure suppresses many unphysical features phenomenological $R(r)$ are subject to. In addition,

TABLE VII. Same as Table II but for ^{209}Bi.

E_0 (MeV)	q_{eff} (fm^{-1})	$(d\sigma/d\Omega)_{\text{tot}}$ (mb/sr)	$(d\sigma/d\Omega)_m$ (mb/sr)	$F_T{}^2$
176.3	1.937	$8.35(71)\times10^{-7}$	$3.23(90)\times10^{-7}$	$1.80(50)\times10^{-3}$
182.0	1.999	$4.40(42)\times10^{-7}$	$3.19(53)\times10^{-7}$	$1.90(30)\times10^{-3}$
191.0	2.093	$2.89(26)\times10^{-7}$	$2.18(34)\times10^{-7}$	$1.43(22)\times10^{-3}$
203.7	2.226	$3.56(25)\times10^{-7}$	$1.77(38)\times10^{-7}$	$1.32(28)\times10^{-3}$
221.3	2.413	$1.07(32)\times10^{-7}$	$5.68(1.7)\times10^{-8}$	$5.00(1.5)\times10^{-4}$
230.1	2.505	$5.04(64)\times10^{-8}$	$3.98(66)\times10^{-8}$	$3.80(62)\times10^{-4}$
250.1	2.716	$1.04(35)\times10^{-8}$	$7.96(3.52)\times10^{-9}$	$8.95(3.95)\times10^{-5}$

knowledge of $R(r)$ obtained from other sources can be incorporated. In particular, the large radius behavior of $R(r)$ can be constrained by imposing the experimentally known separation energies. Thereby the well known ambiguity occurring in the determination of rms radii from charge scattering is avoided.

We use the Schrödinger equation for the single particle radial wave function R_α:

$$\left[\epsilon_\alpha+\frac{\hbar^2}{2\mu}\nabla_x{}^2-V(x)-\frac{l(l+1)\hbar^2}{2\mu x^2}\right]R_\alpha(x)=0\ , \tag{5.1}$$

where the reduced mass $\mu=m(A-1/A)$, m is the nucleon mass, and the radial coordinate x is defined relative to the center of mass of R_{A-1} the nucleus $(A-1)$.

Strictly speaking, the construction of the current operator in this basis is complicated because R_{A-1} is not fixed in space. As a consequence the $(A-1)$ core, orbiting around the A-body mass center, contributes to the intrinsic current. We therefore impose a transformation to the shell-model basis by effectively neglecting the $(A-1)$ center of mass motion $(A\to\infty,\ \mu\to m)$. A similar approach has been used by Elton and Swift[21] in the construction of nuclear charge densities in a single-particle wave function basis.

For the local potential $V(x)$, we use a Woods-Saxon shape:

$$V(x)=-V_0 f(x)+V_{\rm so}\left[\frac{\hbar}{m_\pi}\right]^2\frac{1}{x}\frac{d}{dx}f(x)(\vec{l}\cdot\vec{\sigma})+V_C(x)\ , \tag{5.2}$$

where

$$f(x)=\left[1+\exp\left[\frac{x-R}{a}\right]\right]^{-1},\quad R=r_0(A-1)^{1/3}\ ,$$

and the Coulomb potential V_C is due to a uniform sphere of charge whose rms radius is equal to the experimental charge radius.

The number of parameters introduced in this formulation cannot all be determined individually by the present data of limited q range. In order to fix a certain subset of the parameters we make maximum use of the available empirical facts, thus largely avoiding theoretical biases in the analysis. We adopt the following procedure:

(1) For the single particle energy ϵ_α the nucleon separation energy is taken. This ensures a correct behavior of $R(r)$ at large radii (outside the range of the nucleon-nucleus potential).

(2) The spin-orbit potential $V_{\rm so}$ is fixed to the standard value of 7 MeV.[22] This value leads to a correct prediction of the $f_{7/2}$ and $g_{9/2}$ spin-orbit splitting.

(3) The value $a=0.65$ fm, with an estimated error of $\delta a=0.05$ fm, is adopted for the well-diffuseness parameter. This choice is based on two observations: (a) fits to charge scattering cross sections with a charge density constructed from single-particle wave functions calculated in a Woods-Saxon well yield $a=(0.65-0.70)$ fm; (b) optimal overlap of Woods Saxon (WS) and Hartree Fock (HF) Λ-pole magnetic form factors implies $a=(0.55-0.60)$ fm.

The adopted value of a is the standard one[22] used for the bound-state wave functions in the analysis of transfer reactions. The parameter-dependence of the fitted orbital rms radius was investigated in a series of fits to our data. It is found to be very small (see Table VIII).

TABLE VIII. Dependence of the orbital rms radius on the input parameters of the Woods-Saxon well.

Shell	$dr/r/da$ (%/0.05 fm)	$dr/r/dE_s$ (%/MeV)
$1f_{7/2}$	0.62	−0.47
$1g_{9/2}$	0.48	−0.24

Given the present availability of DWBA codes for the calculation of magnetic electron scattering cross sections, the most direct procedure would be to carry out a full DWBA fit. However, in order to economize on computer time, we investigated the applicability of the local-wavelength (or q-effective)

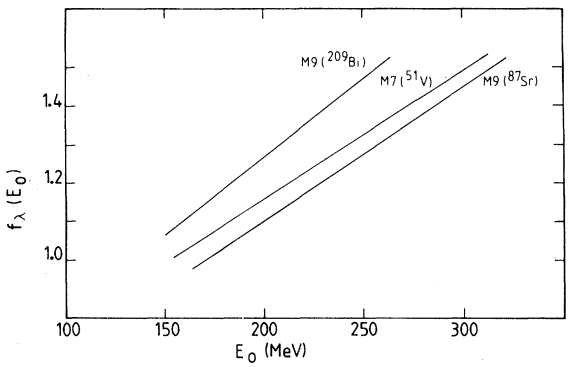

FIG. 9. Phenomenological parameter $f_\lambda(E)$ used to calculate the effective momentum transfer.

approximation

$$q_{\text{eff}}=q\left[1+f_\lambda\frac{Z_\alpha}{R_{eq}E_0}\right],$$

where $R_{eq}=(\frac{5}{3})^{1/2}\langle r^2\rangle_{\text{ch}}^{1/2}$ and f_λ may be a function of multipolarity λ, incoming energy E_0, and possibly the orbital wave function.

In Fig. 9 is shown the E_0 and λ dependence of f_λ for various nuclei. The dependence of f_λ on the orbital wave function was found to be negligible provided that the data do not cover the diffraction minimum of $F_{M\Lambda}(q)$. Its dependence on the multipolarity $\Lambda-2$ is slightly different but does not justify the use of a more complicated approximation.

Based on the arguments given in Sec. II, we adopt the fit functional

$$F_T{}^2(q)=\sum_{J=1}^{\Lambda}\alpha_J{}^2F_{MJ}{}^2(q)*f_{p,n}{}^2(q)*f_{\text{c.m.}}{}^2(q)\ . \tag{5.3}$$

The F_{MJ} are IPSM factors for point nucleons

$$F_{MJ}(q)=N_J^\alpha\{\langle\alpha\,|\,j_{J-1}(qr)\,|\,\alpha\rangle+A_J^\alpha\langle\alpha\,|\,j_{J+1}(qr)\,|\,\alpha\rangle\}\ . \tag{5.4}$$

The factors N_J^α and A_J^α are known functions of multipolarity J, and the quantum numbers $\{\alpha\}$. Here $f_p(q)$ is the nucleon form factor and $f_{\text{c.m.}}(q)$ accounts for the center-of-mass motion of the IPSM wave functions. A four-pole parametrization for $f_p(q)$

$$\left[f_p(q)=\sum_{i=1}^{4}a_i(1+q^2m_i{}^{-2})^{-2}\right]$$

has been used with best-fit parameters[23] deduced from a fit to the proton magnetic form factor. The q dependence of the neutron magnetic form factor $f_n(q)$ is taken to be equal to that of the proton.

The c.m. motion, resulting from the translational noninvariance of shell-model wave functions, can be accounted for in a well defined and simple fashion only in a harmonic oscillator (HO) basis. For a Woods-Saxon basis a better treatment is, in principle, possible with a Gartenhaus-Schwartz transformation.[24] However, the magnitude of the correction, typically $1/A$ of the valence rms radius, does not make the effort worthwhile. Therefore the HO center of mass correction[25] is applied: $f_{\text{c.m.}}(q)=\exp(q^2b^2/4A)$.

B. Fit results

In the fit procedure the two dominating amplitudes α_Λ, $\alpha_{\Lambda-2}$, and the well radius r_0 were varied. For the lower-multipole amplitudes ($J=1$ to $J=\Lambda-4$) the values listed in Table IX have been used. In those cases where low-q experimental data are available (^{51}V, ^{59}Co, ^{93}Nb) the coefficients $\alpha_1-\alpha_{\Lambda-4}$ were fixed to values obtained from a simultaneous fit to all data points.[26] The effect of uncertainties in these values has been treated as a source of systematic error.

For the other cases two types of fits were done: one with $\alpha_1=\alpha_3=\alpha_{\Lambda-4}=\mu_{\text{exp}}\mu_{\text{sp}}{}^{-1}$ (i.e., equal to the quenching of the magnetic dipole moment) and the other with $\alpha_1=\alpha_3=\alpha_{\Lambda-4}=1$. The corresponding differences in the fitted parameters were considered systematic errors and added linearly to the statistical error. The final fits to the magnetic form factor are shown in Fig. 10 (a)–(f). The corresponding best fit Woods-Saxon parameters are quoted on Table X together with the deduced point nucleon orbital rms radii.

The quoted uncertainties for α_Λ, $\alpha_{\Lambda-2}$, and r_0 are only statistical. They are of the order of 5% for α_Λ

TABLE IX. Values of the fixed parameters used in the fits. For an explanation of the entries see text. The α_i ($i<5$) amplitudes for ^{51}V, ^{59}Co, and ^{93}Nb have been taken from Ref. 26.

Nucleus	α_1	α_3	α_5	$-E_S$ (MeV)	$\langle r^2\rangle_{\text{ch}}^{1/2}$ (fm)
^{49}Ti	0.58–1.00	0.58–1.00	free	8.14	3.59
^{51}V	1.28	0.95(6)	free	8.05	3.62
^{59}Co	1.17	0.49(6)	free	7.37	3.78
^{87}Sr	0.57–1.00	0.57–1.00	0.57–1.00	8.43	4.26
^{93}Nb	1.62	0.85(6)	0.50(11)	6.04	4.33
^{209}Bi	1.00–1.56	1.00–1.56	1.00–1.56	3.80	5.52

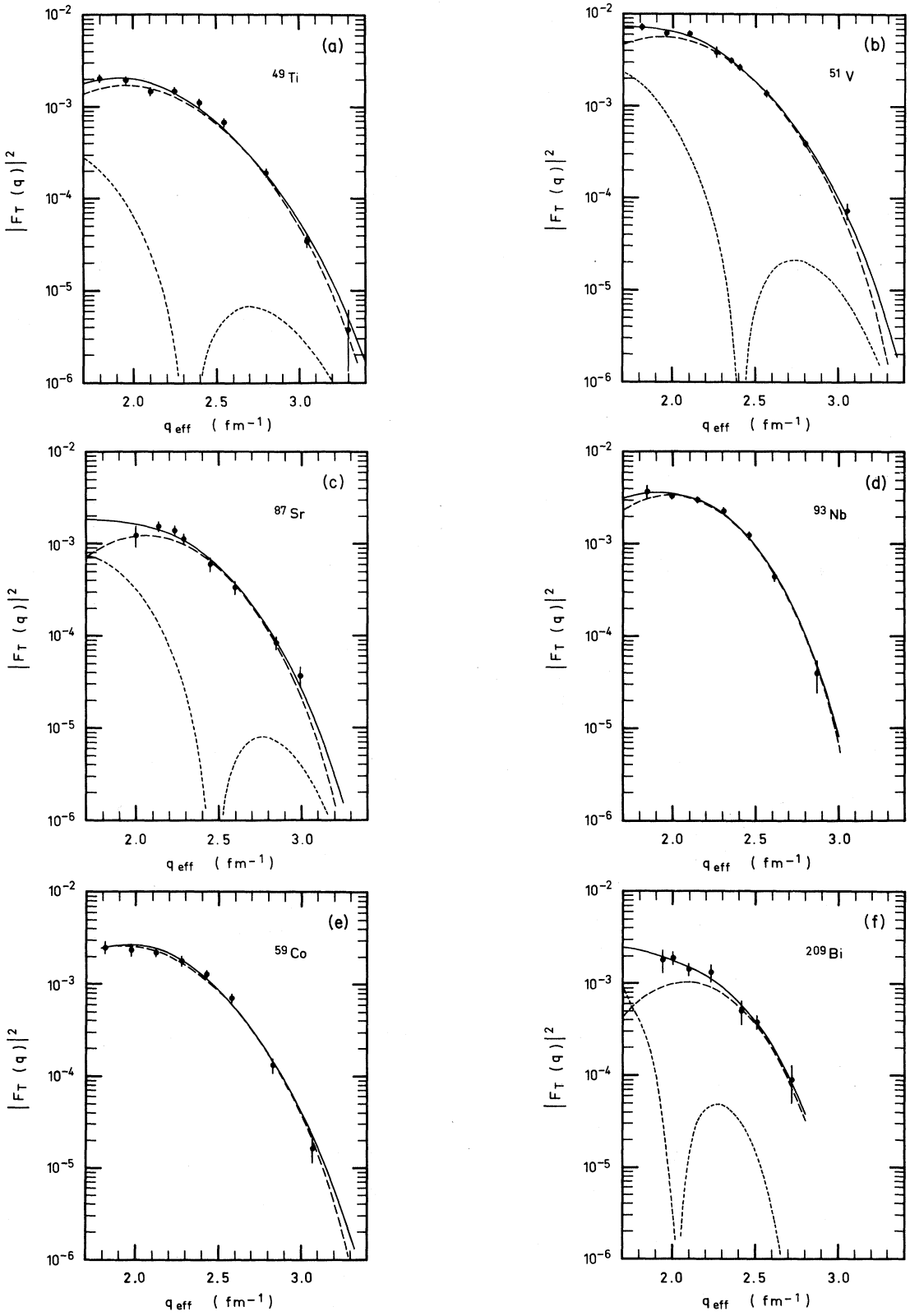

FIG. 10. Woods-Saxon fits (solid line) to the experimental points. The $M\Lambda$ (long dashed) and the $M(\Lambda-2)$ (short dashed) form factors are shown. For ^{59}Co and ^{93}Nb only upper limits exist for the $M(\Lambda-2)$ form factor (see text).

TABLE X. Results of three-parameters fit to the experimental form factors. The errors on the fitted parameters (r_0, $\alpha_{\Lambda-2}$, and α_Λ) are only statistical. The uncertainties of the deduced rms radii include both statistical and systematic errors.

Nucleus	Configuration	$-V_0$ (MeV)	r_0 (fm)	$\alpha_{\Lambda-2}$	α_Λ	$\langle r^2\rangle^{1/2}$ (fm)	$\chi^2/(n-p)$
^{49}Ti	$1f^n_{7/2}$	52.85(53)	1.170(7)	0.55(21)	0.83(4)	3.986(52)	15.9/9
^{51}V	$1f^p_{7/2}$	58.97(51)	1.232(6)	0.86(15)	1.01(3)	4.007(48)	4.9/6
^{59}Co	$1f^P_{7/2}$	59.65(64)	1.173(8)	<0.3	0.69(3)	see text	7.7/6
^{87}Sr	$1g^n_{9/2}$	50.00(99)	1.201(18)	0.89(42)	0.82(6)	4.756(71)	5.8/5
^{93}Nb	$1g^P_{9/2}$	56.82(36)	1.265(8)	<0.4	0.93(3)	4.897(59)	3.5/5
^{209}Bi	$1h^P_{9/2}$	64.5(2.9)	1.199(35)	0.74(20)	0.62(13)	see text	1.3/4

and increase to $\sim 10\%$ if core polarization corrections (see Sec. VI A) are taken into account. Hence the spectroscopic factors obtained have at least the same accuracy as those derived from direct reaction studies. The quantity $\alpha_{\Lambda-2}$ is not well determined due to the small sensitivity of the fit to that parameter. For the case of ^{59}Co and ^{93}Nb the fit essentially forces these amplitudes to zero so that only an upper limit can be given (with a confidence level of 68%). The Bates data[20] for ^{93}Nb are compatible with our measurements and do not have a meaningful influence on the final fit.

The total errors on the rms radii quoted consist of several different components explicitly given in Table XI. The systematic errors come from the uncertainty of parameters fixed in the fit procedure. They also include an estimate of the uncertainty due to the model dependence. The systematic and statistical errors are of the same order of magnitude; their linear sum yields a total error of $1-1.5\,\%$.

We explicitly note here the absence of a quoted rms radius value for both ^{59}Co and ^{209}Bi. The appreciable deformation of the ^{59}Co ground state (see Sec. VII B) precludes a reliable evaluation of the $1f_{7/2}$ orbital rms radius. This is confirmed by the small value for α_7 which indicates that about 30% of the $f_{7/2}$ protons give rise to more complicated configurations. A similarly small spectroscopic factor ($\alpha_9=0.62$) is found for the $1h_{9/2}$ configuration in ^{209}Bi. Unlike ^{59}Co, the ^{209}Bi nucleus is expected to be very rigid (see also Sec. VII B). Nevertheless its jackknife configuration ($J_0=l-\frac{1}{2}$) allows $1\hbar\omega$ excitations to contribute to the $M9$ form factor; the extraction of an rms radius from the measured F_{M9} will require a more detailed study of configuration mixing effects.

The point-nucleon rms radii listed in Table X are calculated in the $(A-1)$ core relative system and thus will be directly comparable to the radii obtained from theoretical calculations. In Table XII we quote in addition the rms radii obtained from an analysis identical to the one described above but with one modification: the omission of the c.m.-correction factor in Eq. (5.3). The resulting Woods-Saxon radial wave functions are then functions of the distance between the nucleon and the c.m. of nucleus A. The rms radii deduced then correspond to the radial extent of $R(r)$ relative to the laboratory-fixed center of mass of the nucleus A. These $R(r)$ are comparable to neutron and pro-

TABLE XI. Different contributions to the quoted errors of experimental rms radii. The systematic errors include the uncertainties on the surface thickness (Δa) and the amplitudes of the lower multipoles ($\Delta\alpha_J$).

Nucleus	Errors (%) Statistical	Systematic $\Delta\alpha_J$	Δa	Total
^{49}Ti	0.43	0.20	0.62	1.3
^{51}V	0.45	0.07	0.62	1.2
^{87}Sr	0.86	0.17	0.48	1.5
^{93}Nb	0.66		0.48	1.2

TABLE XII. Valence rms radii deduced from fit in the center of mass of the nucleus A.

Nucleus	^{49}Ti	^{51}V	^{87}Sr	^{93}Nb
$r_{\rm rms}$	3.943(52)	3.967(48)	4.732(70)	4.882(59)

ton densities obtained from proton or electron scattering.

C. Relative size of n and p orbits

For an accurate test of theoretical calculations, it would be desirable to experimentally determine both the proton and neutron valence shell radii without any model assumptions for the radial wave function $R(r)$. Here the question of a proton or neutron halo in $N \neq Z$ nuclei is directly addressed. This difference can be expected to provide a stringent test for mean field theories; the absolute radii are a function of the adjustments of the effective NN force fitted to experimental proton radial distributions.

This radius difference can be extracted directly from the experimental form factors, without the need of an intermediate step through phenomenological wave function $R(r)$ fitted to the data. From such a direct comparison the uncertainties due to a number of effects, such as the model dependence of $R(r)$, systematic experimental errors, and meson exchange current (MEC) corrections, are reduced or eliminated.

Of course, electron scattering can determine proton and neutron valence shell radii in neighboring, but not the same, nuclei only. As a consequence, the comparison with theory also must be carried out from the same pair of nuclei. In essence, however, the relative extension of neutron and proton orbits still can be determined in a uniquely quantitative way.

From mean field theory, or calculations using Woods-Saxon potentials, we know that for a given shell proton and neutron radial wave functions differ very little in shape. Except for the region where r is large (which will be discussed below) the wave functions are distinguished mainly by a change in radial scale of a few percent. They will be therefore related by the equation

$$R_p(r) = R_n(\beta \cdot r)\beta^{-3/2} . \tag{5.5}$$

The factor β is a number close to one that accounts

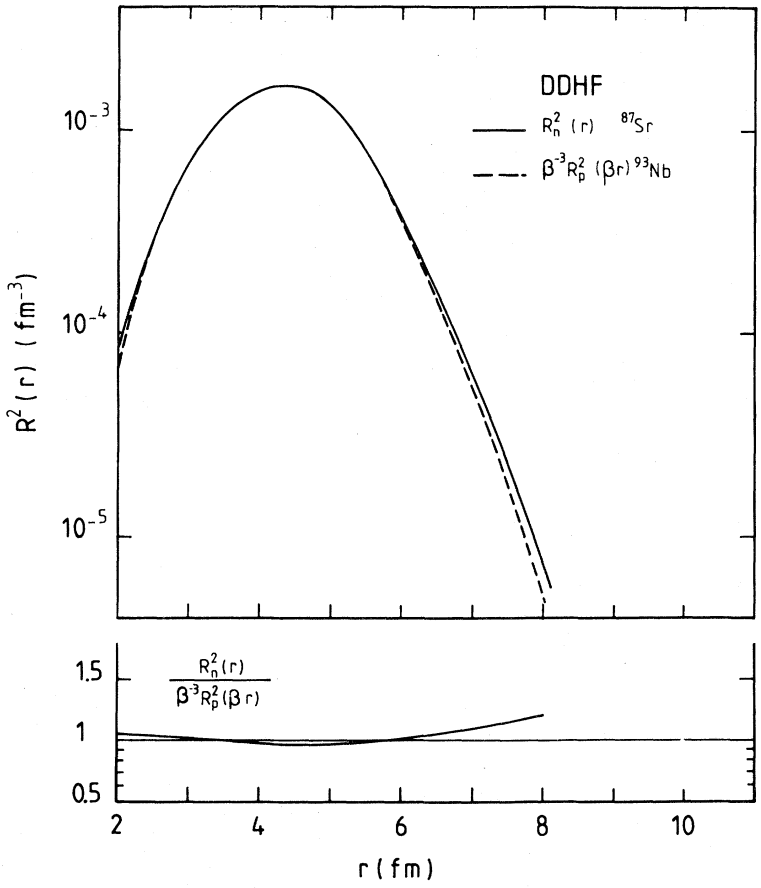

FIG. 11. Check of the "compression" procedure (see text) using mean field predictions (Ref. 27) for $R(r)$. The ratio between the neutron and the compressed proton wave function is shown in the lower part of the figure.

for the compression (dilatation) of the radial scale needed when trying to transform a proton into a neutron wave function. If Eq. (5.5) applies, then we can obtain immediately

$$F_q(q)=F_n(q/\beta)\frac{\alpha_p\mu_p}{\alpha_n\mu_n} . \quad (5.6)$$

A change in radial scale by a factor β is equivalent to a change in q scale by a factor β^{-1}. The remaining scaling factor in Eq. (5.6) is due to the different magnetic moments μ and occupation numbers α for protons and neutrons. Determining β^{-1} by matching, with a compression in q scale, the shape of F_n and F_p yields the difference in radial scale without any model assumption on $R(r)$ other than Eq. (5.5).

In the nuclear interior theoretical wave functions fulfill Eq. (5.5) exceedingly well (see Fig. 11). This is not the case for the tail region, where the falloff $R(r)$ is determined by the separation energies (see Fig. 11). The corrections for this deviation from Eq. (5.5) are quite small ($\sim 1\%$), and can be performed easily as they do not influence the shape of $F(q)$ in the region $1.8-3$ fm^{-1} where our data have been measured. The large-r behavior of $R(r)$ influences the experimental form factor in the low-q region only.

In order to calculate the effect of the improper treatment of the tail by Eq. (5.5), we have compared the rms radii of wave functions that are identical in the nuclear interior ($r<6$ fm), but have different tails outside. The resulting difference of, e.g., 0.9% for the ^{87}Sr/^{93}Nb pair is used to convert the β into a ratio of rms radii denoted β^*. This correction (as well as the compression approach in general) was verified by starting from density dependent Hartree-Fock-Bogoliubov (DDHFB) wave functions[27] for ^{49}Ti and ^{51}V, calculating $F_{M7}(q)$, fitting them to each other using the compression procedure described below, and comparing the resulting β^* to the ratio of the rms radii of the DDHFB wave functions.

For the fit of one set of experimental form factors $F_p^{\rm ex}(q_i)$ to a second one $F_n^{\rm ex}(\beta q_j)$ with β as free parameter, the experimental values of F_p at the momentum transfer βq_j are needed. They are obtained by taking a WS-fit value $F_p^{\rm WS}(\beta q_j)$ and adding to it $F_p^{\rm ex}(q)-F_p^{\rm WS}(q)$ interpolated between neighboring values of q_j. This procedure amounts to an interpolation of $F_p^{\rm ex}(q)$, where the linear term is taken directly from the experimental data while higher order terms are taken from the WS fit. In the fitting procedure, contributions from the $\lambda<\Lambda$ multipoles have been included, but their effect on β was quite small. The resulting values for the ratio of rms radii, already corrected for the different tails of R_n and R_p, are given in Table XIII. The systematic uncertainties on β are very small. The MEC corrections cancel to within 0.4%.

TABLE XIII. Compression factors as deduced from direct comparison of the experimental data. The asterisk indicates that the correction for different asymptotic tails of the proton and neutron wave functions has been made. In the last column the compression factors take into account the effect of the meson exchange currents.

Ratio	β	β^*	$\beta^*_{\rm MEC}$
^{49}T/^{51}V	0.965	0.980(10)	0.980(10)
^{87}Sr/^{93}Nb	0.954	0.964(10)	0.968(10)

Figure 12 shows for ^{49}Ti/^{51}V and ^{87}Sr/^{93}Nb the comparison of the proton and neutron $M\Lambda$ form factors, the latter one being plotted on a compressed q scale. Clearly, the proton and neutron data points lie on a common $M\Lambda$ curve, hereby justifying Eq. (5.4). The χ^2 per degree of freedom of the fit of neutron proton data points is 12/15 for the Ti/V pair and 15/14 for the Sr/Nb pair.

VI. CORRECTIONS

In this section we discuss the importance of various corrections to the interpretation of our data in terms of the independent particle shell model (IPSM) picture, discussed in Sec. II.

A. Configuration admixtures

Recent calculations of Arita[28] have delineated the influence of one particle-one hole core-polarization

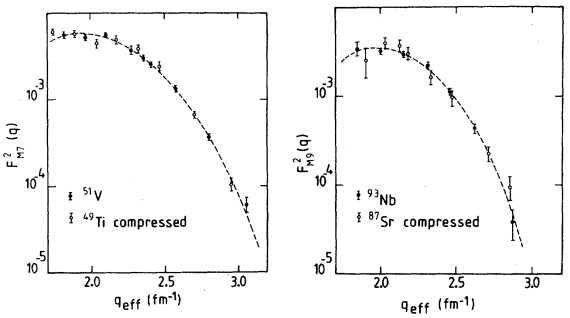

FIG. 12. Comparison between the proton and compressed neutron form factors $F_{M\Lambda}$ for $f_{7/2}$ (a) and $g_{9/2}$ (b) nuclei. Woods-Saxon fits (dashed line) to the odd-proton nuclei were used to subtract lower multipoles and to interpolate ^{49}Ti(^{87}Sr) data between ^{51}V(^{93}Nb) experimental points.

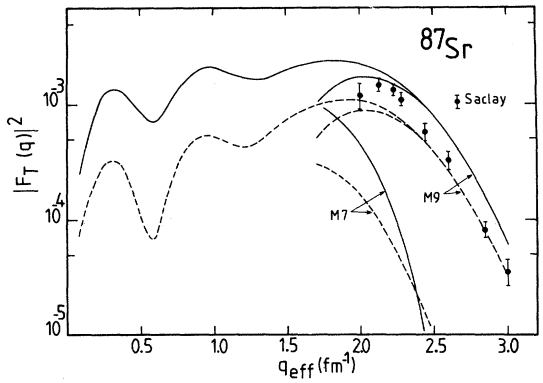

FIG. 13. Dependence of the magnetic form factor of ^{87}Sr on the core polarization effect as calculated in Ref. 28.

on magnetic form factors of ^{87}Sr and ^{51}V in a large configuration space. In first-order perturbation theory the relevant matrix element is given by:

$$\langle \psi_A || \hat{T}^m_J(q) || \psi_A \rangle = \langle \alpha || \hat{T}^m_J(q) || \alpha \rangle - \sum_{\mathrm{ph}J_2} \frac{2}{\Delta E_{\mathrm{ph}}} W(\mathrm{ph}\alpha\alpha; JJ_2) \times \langle \mathrm{ph}J_2 \mid V \mid \alpha h J_2 \rangle \times \langle h || \hat{T}^m_J(q) || p \rangle ,$$

where W accounts for angular momentum couplings. The particle-hole matrix element is calculated using two phenomenological effective interactions V, one with a Rosenfeld and one with a Serber exchange mixture.

The calculated result for ^{87}Sr, obtained with harmonic oscillator radial wave functions ($b=2.00$ fm) and for particle-hole excitations up to $(\Lambda+1)\hbar\omega$ is shown in Fig. 13. The $M7$, $M9$, and total form factors are shown for both the extreme IPSM and the IPSM plus Serber-force core polarization (CP) calculation. The Serber-force calculation is emphasized because it produces a much more pronounced effect on the cross section in the q range considered. One can see that, in spite of the dramatic effect of core polarization on the amplitude of each multipole, the dominance of the $J=9$ multipole in the high-q region is preserved. Also its shape remains practically unchanged; the quenching of the $M\Lambda$ form factor is nearly q independent. A similar calculation for ^{51}V that includes, in addition to polarization of the ^{48}Ca core, also a recoupling of the $(1f_{1/2})^3$ configuration, yields very similar results. In order to put these observations on a more quantitative basis we applied the fit procedure to pseudodata, generated from IPSM and (IPSM + CP) wave functions. The fitted values of the rms radius of the odd-nucleon orbital are found to differ by less than 0.3%.

It is important to note that the observed model independence of the radius-extraction procedure to core polarization effects is a systematic one that occurs for such widely different nuclei as ^{51}V, ^{87}Sr, and ^{209}Bi.

Although the model used[28] might be considered crude and the application of first-order perturbation theory open to improvements, it is reassuring that this model reproduces almost quantitatively the feature of a strong quenching of the $M3$ and $M5$ form factors observed in various nuclei.[26] Moreover, a recent calculation[29] of magnetic form factors in permanently deformed nuclei indicates that the $J<\Lambda$ components are strongly reduced and changed in shape, while $F_{M\Lambda}(q)$ is again dominant in the relevant q range and has almost identical q dependence.

Recently Donnelly and Gokalp[30] studied the effect of configuration mixing on the magnetic form factors of ^{49}Ti, ^{59}Co, ^{87}Sr, and ^{93}Nb. They used two-hole one-particle and three-particle admixtures to the ground state wave function. The coefficients of these admixtures have been fitted to our high momentum transfer data and to the experimental magnetic moments. Their results for α_Λ are in agreement with the α_Λ found in this work and show that the shape of the highest multipole is very weakly changed by configuration admixtures. At the same time huge differences are observed for lower multipoles. Donnelly and Gokalp have also investigated the model dependence of the extracted wave functions. Their results show that for all possible admixtures, the valence rms radius would vary within 2%. However, for ^{51}V and ^{93}Nb, where low and medium momentum transfer data exist, the uncertainty is much smaller. It is lower than 0.5% for ^{93}Nb, where the magnetic form factor is known between 0.5 and 3.0 fm^{-1}. Our fit (to the highest q points only) gives a value for the rms radius within that uncertainty. For ^{49}Ti and ^{87}Sr we expect similar agreement. However, low and medium momentum transfer data will be needed to reach the same degree of confidence in the experimental uncertainty of the rms radius.

In conclusion, the extreme-IPSM interpretation of Λ-pole magnetic form factors remains, in essence, valid in the presence of wave function admixtures of the scope discussed here.

An additional point, not yet discussed, concerns the characterization of a given ground state configuration as a proton or a neutron single particle state.[31] If for a specific single-particle proton state the corresponding neutron shell is closed (or vice versa) the state has good isospin. In the extreme IPSM approximation this condition is satisfied for all nuclei considered, except ^{49}Ti. In the general case, when the core-polarization mechanism breaks shell closures, the requirement of good isospin imposes an admixture of proton and neutron states in the total wave function. Although the extent to which the present interpretation will be affected by the condition of good isospin remains to be calculated, the near equality of proton and neutron orbital rms radii makes the effect probably of minor importance.

B. Meson exchange currents

Because of the very steep falloff of the one-body form factor at large q, any mechanism which allows two or more nucleons to share the momentum transferred by the virtual photon becomes increasingly important. The dominant mechanism in transverse scattering is the meson exchange currents (MEC). In the momentum-transfer range considered here ($q \lesssim 3$ fm^{-1}) the one-pion exchange diagrams[32] are the dominant pieces. They correspond to two-body terms $\hat{F}_T^{(2)}$ in the magnetic operator that modify the one-body form factor schematically as follows:

$$F_T^2(q) \propto |\langle \alpha | \hat{F}_T^{(1)} + \hat{F}_T^{(2)} | \alpha \rangle|^2 = |F_T^{(1)} + F_T^{(2)}|^2 .$$

In the q region of our experiment $|F_T^{(2)}|^2$ is much smaller than $|F_T^{(1)}|^2$; therefore the major part of the correction will come from the cross term $2F_T^{(1)} \cdot F_T^{(2)}$.

Recently Suzuki *et al.*[33] and Dubach[34] performed extensive calculations of the modification of single-particle magnetic form factors due to the MEC contribution. These calculations involve the evaluation of the one-pion exchange diagrams with a nonrelativistic reduction scheme. Suzuki has, in addition, included the first-order core-polarization mechanism in the calculation.

The MEC contributions calculated by Suzuki are obtained using a harmonic oscillator (HO) radial basis while our data are interpreted using WS wave functions. Direct application of his results in q space then leads to an inconsistency, due to the different shapes of the form factors involved. In order to avoid such problems we express the MEC effect, as calculated in an HO basis, in terms of the relative change of the orbital rms radius. Using the calculations of Suzuki *et al.*, for MEC, fits were made to various sets of $F_{M\Lambda}$ pseudodata (with realistic error bars) both without and with inclusion of the two-body current operator. A parametrization of the πNN form factor,[35] occurring in the two-body operator (see below), was also included in the fits. It turns out that the relative change of the orbital radius is practically constant when b is varied within reasonable bounds. This property justifies the application of the same correction to results obtained in terms of one-body form factors and in a Woods-Saxon basis. The results are summarized in Table XIV. It is important to note that the MEC correction cancels to a large extent in the ratio of proton to neutron radius. The amplitude factors α_Λ are modified appreciably by the MEC correction but are rather insensitive to the choice of $F_{\pi NN}$ ($\pm 2\%$).

TABLE XIV. Effect of the MEC corrections (Ref. 32) on $r_{\rm rms}$ and α_Λ calculated in a harmonic oscillator basis.

Configuration	$1f^n_{7/2}$	$1f^p_{7/2}$	$1g^n_{9/2}$	$1g^p_{9/2}$
$\frac{\Delta r}{r}$ (%)	1.4	1.4	1.4	1.0
$\frac{\Delta\alpha_\Lambda}{\alpha_\Lambda}$ (%)	−9	−8	−7	−7

We note in passing that good fits to "effective" (including MEC) form factors can be obtained; this unfortunately implies that for this work the MEC effect has no unique signature in the limited q range below $q \lesssim 3$ fm^{-1}.

The MEC contributions[33,34] have been applied to Hartree-Fock form factors in the literature. Their effect on $F_{M\Lambda}(q)$ or the orbital rms radius is often larger than the one given in Table XIV. This is due to two important shortcomings.

First, it is necessary to calculate MEC using a value of the oscillator parameter such that one-body HF-form factor $F_{M\Lambda}^{(1)}$ (HF) is closely matched by $F_{M\Lambda}^{(1)}$ (HO). The resulting value for b does not necessarily match the one obtained from the total nuclear charge density or from minimization of the total HF energy. In Fig. 14 is shown that the choice[33] of b $(1g_{9/2})=2.0$ fm leads to a gross mismatch of $F_{M9}^{(1)}$ (HF) and $F_{M9}^{(1)}$ (HO). As a conse-

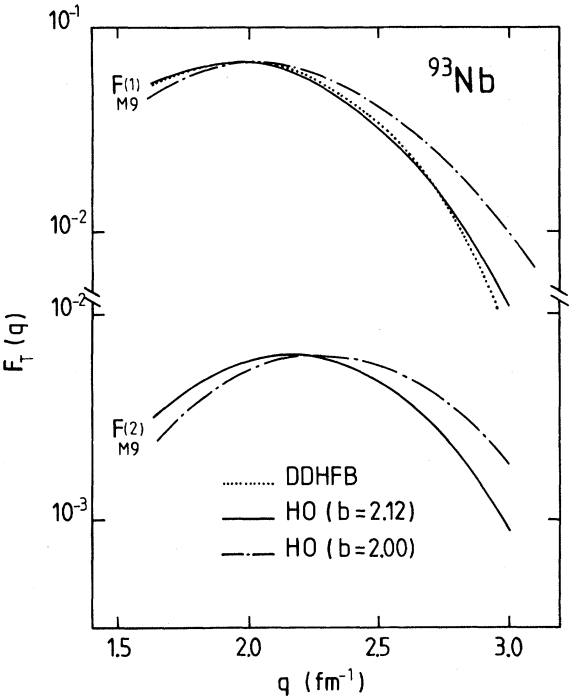

FIG. 14. One- and two-body magnetic form factors of ^{93}Nb. The DDHFB one-body $M9$ contribution (dotted line) is compared to HO calculations with $b=2.00$ fm (dashed line) and $b=2.12$ fm (solid line).

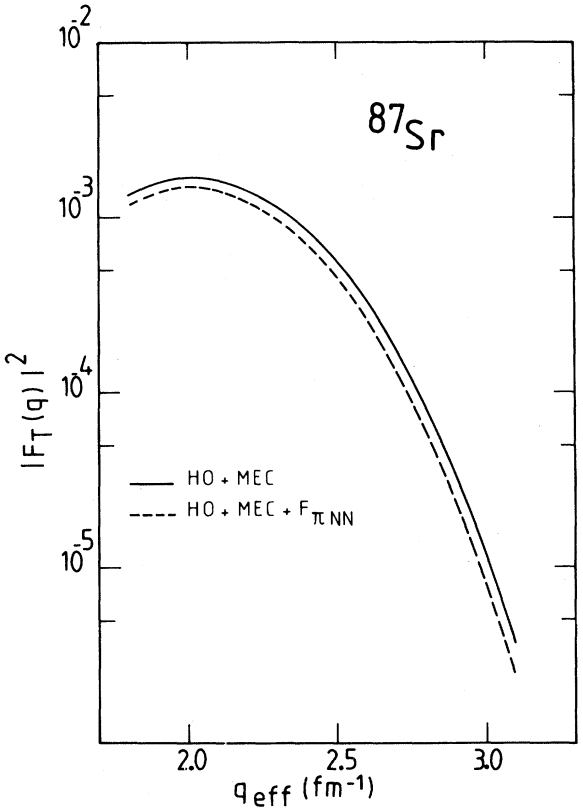

FIG. 15. Effect of the πNN vertex form factor on the MEC calculations. The solid line shows the magnetic form factor of ^{87}Sr as calculated in Ref. 27 with MEC included. The dashed line shows the same calculation with the πNN vertex form factor included.

quence the $F^{(2)}_{M9}$ is too large as well. Owing to the steep falloff of $F^{(1)}_{M9}$ the MEC-corrected HF form factor overshoots appreciably. An appropriate choice of $b=2.12$ fm leads to a better overlap between the one-body form factors and to a much smaller effect of $F^{(2)}$ at very large q.

In spite of the fact that the MEC mechanism contains the inverse pion mass as a length parameter it turns out that $F^{(2)}_{M\Lambda}$ is to a good approximation a function of (qb) only.[33] This property allows a scaling of $F^{(2)}_{M\Lambda}$ in a simple way to the appropriate value of b. The result of the adapted calculation is shown in Fig. 14.

The second, more fundamental, point concerns the often encountered neglect of the πNN-vertex form factor $F_{\pi NN}(k^2)$. At large values of the momentum k transferred at the π-N vertex, this form factor reduces the MEC contribution by 10–40%.[33] Some uncertainty exists about the correct form of $F_{\pi NN}$. Erkelenz[35] argues that in the parametrization given by

$$F_{\pi NN}(k^2)=[(\lambda^2-m_\pi{}^2)/(\lambda^2+k^2)]^{1/2}$$

a cutoff mass $\lambda \geq 7m_\pi$ should be adopted. Alternatively, Lock and Foldy[36] propose that $\lambda=5m_\pi$ should be employed. In Fig. 15 the above effect of the πNN vertex on the total form factor is shown for the case of ^{87}Sr. The uncertainty on the cutoff mass (we choose $\lambda=5\pm2$) m_π leads to the errors quoted in Table XIV.

In summary, the MEC contributions lead to a change of the extracted rms radii of 1–1.4%. However, new calculations by Desplanques and Mathiot[37] show that further understanding of these processes (use of Hartree-Fock wave functions, short range NN correlations) is needed before truly quantitative corrections can be applied.

VII. COMPARISON WITH SELF-CONSISTENT CALCULATIONS

This section is devoted to the comparison of our experimental results with the predictions of mean field theories. Considerable progress has been achieved in the last few years in the theoretical

description of finite nuclei, essentially on the basis of the G-matrix formalism developed by Brueckner.[38] The calculations now available predict quite well the bulk properties of the nucleus (saturation properties, charge rms radii). A more stringent test of the validity of the mean field theories results from the comparison with experimental charge densities. Such a comparison is meaningful in particular when electron scattering experiments are extended to sufficiently high momentum transfer,[17] so that the density in the interior of the nucleus is measured as well.

The mean field predictions for the total proton or neutron distributions result from a sum over single particle densities. Up to now no significant comparison has been possible for the individual components of the total densities, mainly due to the lack of precision on the experimental radial wave functions. Experiments using hadronic probes are sensitive mainly to the surface and the tail region of the densities. With magnetic electron scattering we can probe the region where the valence nucleon density is large, thus providing a new and accurate test for the predictions of the mean field theories.

It is beyond the scope of the present work to describe the various self-consistent calculations now available. Recent articles by Dechargé and Gogny,[39] Quentin and Flocard,[40] Svenne,[41] and Goodman[42] summarize the present understanding of the nucleus in the frame of the mean field theories. For clarity we shall only outline the main features of the different calculations used for comparison with the experimental data.

A. Theories

In most approaches to mean field theory, the Brueckner G matrix is derived from a Reid soft-core nucleon-nucleon potential. The local density approximation is applied to transform the nuclear-matter G matrix into a density dependent effective force to be used in finite nuclei.[43] Campi and Sprung[44] use the Sprung-Banerjee[45] parametrization of the effective force to solve the Hartree-Fock equations in coordinate space. This calculation has been extended to open shell nuclei using the filling approximation and the Bardeen-Cooper-Schrieffer (BCS) equations to determine the number of particles in each orbit. We shall refer to the Campi-Sprung calculations as DDHF (density dependent Hartree-Fock).

A simplified calculation involving a first order expansion of the nuclear density matrix was performed by Negele and Vautherin.[46] They showed that retaining only the lowest terms yields physical results that are essentially the same as those obtained in the full density dependent Hartree-Fock calculation, previously performed by Negele.[43] Both the DDHF and the density matrix expansion (DME) methods need phenomenological adjustments of some constants of the effective interaction in order to account for higher order effects.

A self-consistent approach which includes the pairing correlations between nucleons was developed by Dechargé and Gogny.[39] They used the Gogny $D1$ density dependent effective interaction[47] which was especially designed for complete Hartree-Fock Bogoliubov calculations. The coefficients of the interaction are fitted to the bulk properties of ^{16}O and ^{90}Zr and to the pairing properties of ^{116}Sn. In order to keep the full self-consistency of the calculation this is a finite range force; further extension such as the inclusion of the random phase approximation or collective degrees of freedom are hence possible without any change of the parameters of the force. In particular, Dechargé and Gogny simultaneously derive the Hartree-Fock field and the pairing field with the same force. We shall denote this calculation as DDHFB (density dependent Hartree-Fock-Bogoliubov).

For the sake of completeness the comparison between theory and experiment will be made both in momentum space and in configuration space. The MEC as described in Sec. VI will be taken into account before drawing quantitative conclusions.

B. Comparison with experimental data

The theoretical form factors[27,44,46] calculated using expression (2.5) are shown in Fig. 16 (a)—(f) together with the experimental points. Differences between experiment and theory can be characterized by two features: the overall normalization of the predictions relative to experiment and the shape of the $F_{M\Lambda}$ contribution.

The relative normalization can be defined as the ratio between experiment and theory in the region where the Λ-pole form factors reach their maximum. One observes that the agreement with the experiment depends strongly on the nucleus studied. This is easily explained by the fact that mean field theories do not account for configuration mixing. If such mixing occurs a smaller number of particles are present in the valence orbit and the amplitude of the corresponding Λ-pole form factor is reduced.

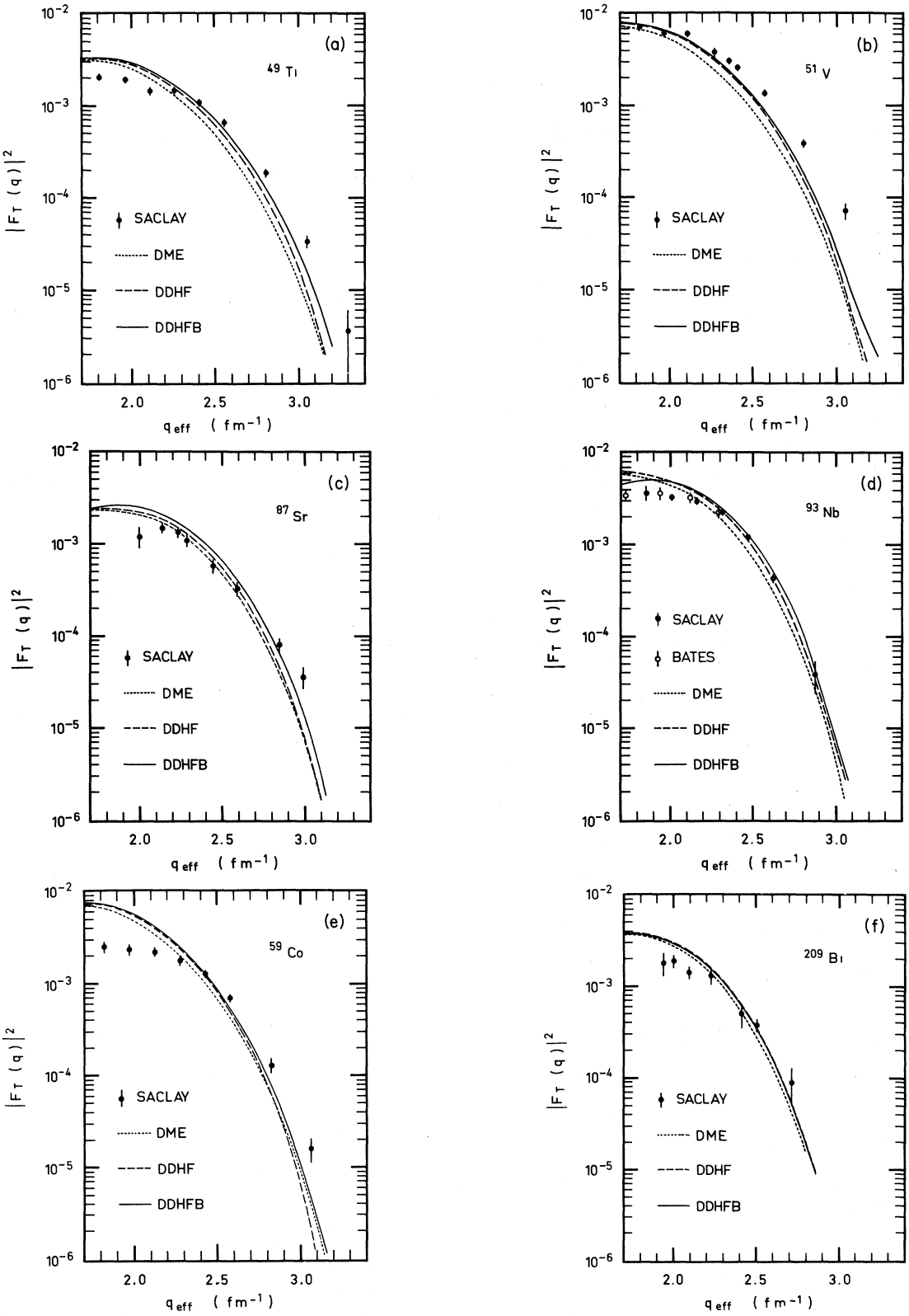

FIG. 16. Experimental form factors compared to DME (dotted line, Ref. 46), DDHF (dashed line, Ref. 44), and DDHFB (solid line, Ref. 27) self-consistent calculations.

Hence the good agreement for ^{51}V indicates that the configuration of one unpaired proton in the $1f_{7/2}$ orbit is very close to that experimentally measured. A small disagreement is observed for ^{49}Ti showing that some configuration admixtures must be added to the strict single particle (or quasiparticle in DDHFB) picture. Similar remarks can be made for ^{87}Sr, ^{93}Nb, and ^{209}Bi nuclei. The disagreement in amplitude is very pronounced for ^{59}Co; here the mean field theories strongly overestimate the $f_{7/2}$ single particle contribution to the ground state wave function. Quantitatively these observations are related to the spectroscopic factors α_Λ determined experimentally and describing the single particle contribution to the measured Λ-pole form factor. In first approximation the values of α_Λ obtained in Sec. V are the coefficients needed to renormalize the calculated curves in order to obtain better agreement with the experiment. This is partly explained by the depletion of the corresponding orbitals due to the core polarization effect, not taken into account in the calculations cited.

The most important information is contained in the q dependence (the shape of the form factor). Indeed it is the shape of the highest multipole (dominant in the region of interest) which is determined by the radial extension of the valence orbit studied. As a general feature we observe that the predicted form factors fall off too rapidly in the high-q region. Because the radial part of the valence orbit corresponds to the Fourier-Bessel transform of the Λ-pole moment this is a signature of too large a radial extension for the calculated wave functions. Only for ^{93}Nb do the experimental and theoretical form factors have quite similar behavior. It is also observed that in most cases DDHFB predicts slightly better shapes of the form factors than DME or DDHF.

The same qualitative features are observed by comparing the wave functions in coordinate space. As an illustration we show the $1f_{7/2}$ neutron orbit of the ^{49}Ti nucleus (Fig. 17). The best Woods-Saxon fit is displayed together with the three theoretical curves. All calculations predict wave functions peaked at radii larger than the ones experimentally found. Moreover, the discrepancies observed in q space are confirmed: The steeper falloff of the form factor comes from a larger radial extension in coordinate space.

Part of the above discrepancies are due to the fact that mean field calculations do not include mesonic degrees of freedom. As shown by Dubach[34] and Suzuki *et al.*,[33] the inclusion of a two-body term in

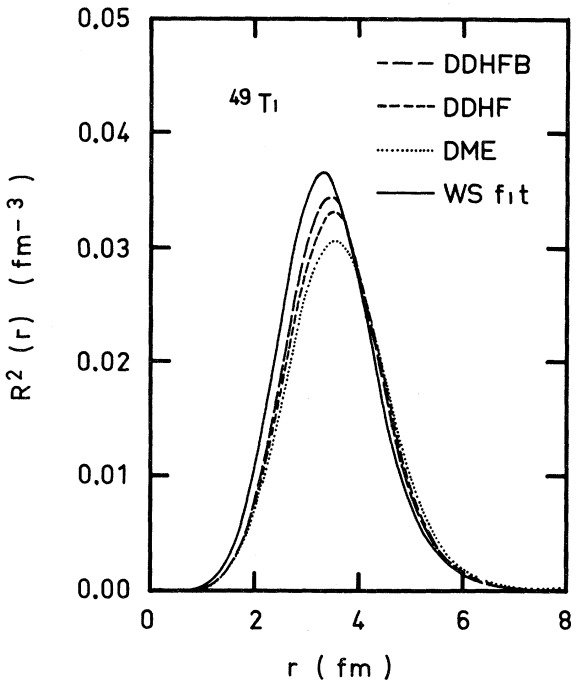

FIG. 17. $1f_{7/2}$ neutron wave functions of ^{49}Ti. The WS fit (solid line) is compared to DME (dotted), DDHF (short dashed), and DDHFB (long dashed) calculations.

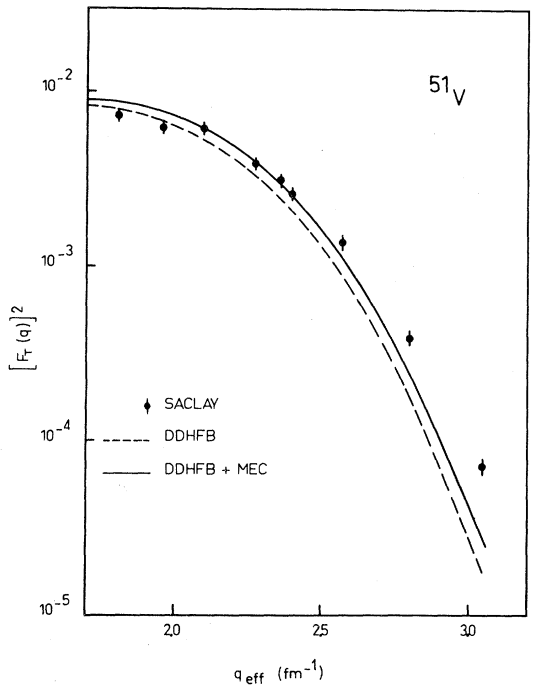

FIG. 18. ^{51}V magnetic form factor. The theoretical curve (dashed) calculated with DDHFB wave function includes the MEC contribution of Ref. 33. The appropriate HO constant was chosen and the πNN vertex form factor was taken into account.

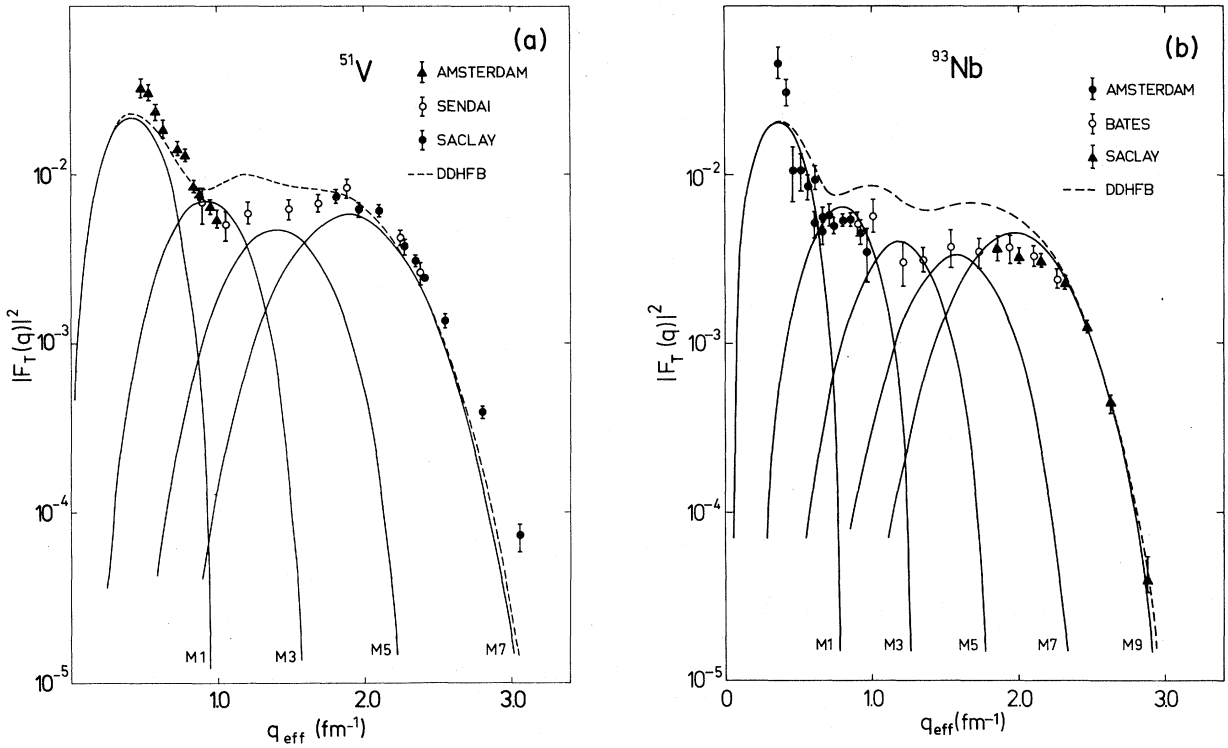

FIG. 19. Magnetic form factors of (a) ^{51}V and (b) ^{93}Nb. Data comes from Amsterdam (Refs. 48 for ^{51}V and 49 for ^{93}Nb), Sendai (Ref. 19), Bates (Ref. 20), and Saclay (present work). The Hartree-Fock calculation is from Ref. 27. For clarity only first maxima of each multipole are shown (solid lines). The dashed lines represent the total magnetic form factor.

the current operator induces a significant contribution to the form factor for higher q values. This leads to an improved agreement with the experiment, as shown in Fig. 18 for ^{51}V. Here the DDHFB prediction was corrected for the MEC effect as calculated in Ref. 33. For this comparison we have included the effect of the πNN vertex form factor and the two-body contribution was scaled to the appropriate harmonic oscillator parameter. The shape of the predicted form factor is now somewhat closer to the shape of that experimentally measured. Quite similar results are found for ^{49}Ti, ^{59}Co, and ^{87}Sr nuclei, while for ^{93}Nb the inclusion of MEC slightly deteriorates the agreement with the data.

For two of the nuclei studied, namely ^{51}V and ^{93}Nb, the data now cover the whole region between 0.5 and 3.0 fm^{-1}. For each of them the measurements come from three different laboratories. The agreement among the different sets of data in the region where they overlap [Fig. 19 (a) and (b)] is very good. The comparison with Hartree-Fock calculations shows that in the medium momentum transfer region the experimental data are lower than the theoretical curves. This observation confirms the previous result for ^{17}O (Ref. 84) where the $M3$ multipole was found to be strongly quenched. Part of the discrepancy observed can be removed by including core polarization and meson exchange current effects. Further investigations will, however, be required to explain both the amplitude and the shape of the experimental magnetic form factor over the whole range of momentum transfer studied.

As discussed in Sec. V, for nuclei having a sufficiently pure single particle configuration (^{49}Ti, ^{51}V, ^{87}Sr, ^{93}Nb), the experimental data can be interpreted in terms of the radial densities of valence nucleons. At this point we note that there is a distinction between the particle density of Hartree-Fock calculations (DME, DDHF) and the quasiparticle density of a Hartree-Fock-Bogoliubov calculation. Pairing correlations introduce a term which depends on the time reversal properties of the operator involved in the reaction mechanism. A quasiparticle is defined as a linear sum over creation and annihilation operators with amplitudes U_n and V_n.[39] The quantity $R^2(r)$ probed by the experiment is therefore given by:

TABLE XV. Theoretical and experimental point nucleon valence rms radii. In the last column the MEC corrected experimental values are quoted.

Nucleus	Orbit	Valence radius (fm) DME	DDHF	DDHFB	WS	WS + MEC
^{49}Ti	$1f^{n}_{7/2}$	4.210	4.124	4.068	3.986(51)	4.042(56)
^{51}V	$1f^{p}_{7/2}$	4.246	4.140	4.107	4.007(48)	4.063(53)
^{87}Sr	$1g^{n}_{9/2}$	4.946	4.880	4.832	4.756(72)	4.823(76)
^{93}Nb	$1g^{p}_{9/2}$	5.047	4.954	4.931	4.897(58)	4.946(64)

$$R^2(r)=\sum_{n,n}[U_n(lj)U_{n'}(lj)-\epsilon V_n(lj)V_{n'}(lj)]R_n^{lj}(r)R_{n'}^{lj}(r)\ , \tag{7.1}$$

where n and n' are the radial quantum numbers. For charge scattering $\epsilon=-1$, whereas $\epsilon=+1$ in the case of magnetic scattering. The difference between radial densities deduced from charge or magnetic scattering experiments depends on the strength of the pairing correlations. For the nuclei studied here a change of the sign of ϵ amounts to a few percent change in the rms radius of $R(r)$. Hartree-Fock calculations (without pairing correlations) do not differentiate between charge and magnetic scattering. However, the rms radius derived from such a calculation is very close to the "magnetization" valence radius obtained in a complete Hartree-Fock-Bogoliubov calculation. This is due to the normalization condition on U_n and V_n $[\sum_n(U_n{}^2+V_n{}^2)=1]$ and to the positive sign in expression (7.1) for the case of a magnetic current operator. For the same reason a non-negligible difference occurs between the Hartree-Fock radius and the Hartree-Fock-Bogoliubov "charge" valence radius.

All measured and calculated valence rms radii are quoted in Table XV. A systematic trend is observed: The predicted radii slightly overestimate the experimental values. This is shown in Fig. 20, where the relative differences between theory and experiment are plotted. When MEC corrections are taken into account (see Sec. VI B) the agreement between the predicted and measured valence rms radii is improved by less than 1%.

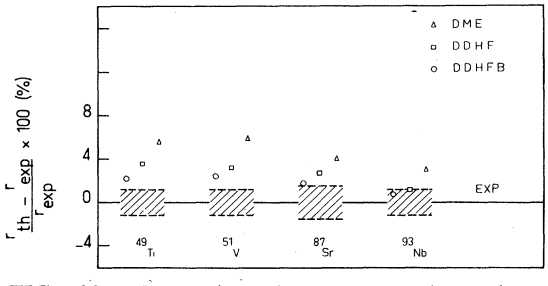

FIG. 20. Comparison between experimental and theoretical rms valence radii. The dashed lines correspond to the uncertainties of the experimental values.

For completeness we also consider the Hartree-Fock separation energies E_s. These E_s determine the asymptotic tail of the valence orbital, and are therefore related to the corresponding rms radii. We have compared the experimental E_s (as used in our Woods-Saxon parametrization) with the calculated separation energies given by $E_s=E_A-E_{A-1}$, E_A being the binding energy of the nucleus A. (Comparison of the single particle Hartree-Fock energies with the experimental E_s would lead to erroneous conclusions.) We have found that DDHFB $f_{7/2}$ and $g_{9/2}$ separation energies agree to within 0.3 MeV with the experimental values, while DME and DDHF predict E_s to be 0.5 to 3 MeV larger. We also note that if these calculations are modified to improve agreement with the experimental separation energies, then the discrepancies between calculated and measured rms radii are increased by as much as 1.5%.

In Table XVI we have collected the charge density rms radii of the nuclei studied. A fairly good agreement (within 1%) between theory[39,44,46] and experiment[2,49,50] is observed for all nuclei. Since charge radii are global quantities, used to fit phenomenological forces, such agreement is quite natural.

Some complementary information is contained in the deformation energy surfaces[51] of the nuclei of

TABLE XVI. Theoretical and experimental charge rms radii. Experimental values are taken from Refs. 2, 49, and 50.

Nucleus	Charge radius (fm) DME	DDHF	DDHFB	EXP
^{49}Ti	3.588	3.546	3.562	3.580±0.005
^{51}V	3.627	3.584	3.597	3.605±0.005
^{87}Sr	4.225	4.184	4.203	4.215±0.003
^{93}Nb	4.331	4.269	4.289	4.318±0.009

interest. For nuclei with well defined deep minima, quite a good theoretical description of their ground state is expected. This is obviously the case for the ^{87}Sr and ^{93}Nb nuclei, as shown in Fig. 21. Some additional components may be present in the ground state wave functions of the less rigid nuclei ^{49}Ti and ^{51}V. The ^{59}Co nucleus is very soft against deformation; this suggests that deformed components must be included in order to obtain better agreement with the experimental data. A single particle interpretation for ^{59}Co therefore would not be appropriate. The situation is quite different for ^{209}Bi: The sharp minimum of its potential energy indicates a very rigid nucleus. However, the $J_0=l-\frac{1}{2}$ configuration of its ground state allows contributions of $1\hbar\omega$ excitations to the $M9$ magnetic multipole. A proper estimation of these contributions is needed before really quantitative discussion in terms of radial wave functions can be performed.

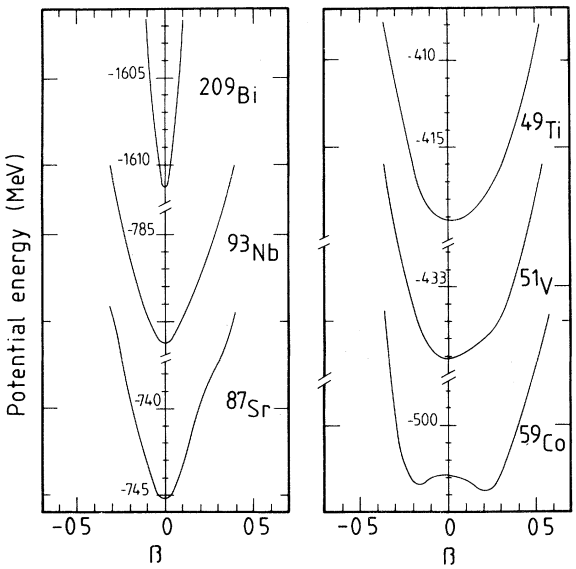

FIG. 21. Potential energy surfaces versus deformation parameter, as calculated in DDHFB (Ref. 51).

VIII. COMPARISON WITH OTHER EXPERIMENTS

Having determined very precisely the radial extension of valence-nucleon orbitals, we would like to compare our results with those obtained from other experimental techniques. We believe that such a comparison will allow a better estimation of the validity of the model used in each of the approaches considered.

There exists a wide variety of experiments which aim at a determination of proton or neutron radial densities. But, for our purpose it will be sufficient to restrict the comparison to a few typical results involving different probes. First, we will discuss the results from two types of measurements using the electromagnetic interaction, the isotone charge density differences, and the Coulomb-energy differences. The discussion of experiments involving hadronic probes will include results from transfer reactions and high energy proton elastic scattering.

A. Charge density differences of isotones

Electron scattering experiments from isotone pairs determine the charge density difference of the two nuclei involved. This charge density difference can be related to the radial density of the valence protons. In this section we will compare the results obtained by this method to those determined from magnetic electron scattering, corrected for meson exchange, finite nucleon size, and center-of-mass effects.

The experimental isotone charge density difference, defined as $\Delta\rho=\rho(N,Z_1)-\rho(N,Z_2)$, can be related to the valence density $R_{\rm ch}^2(r)$, provided that the core polarization $\Delta\rho_{\rm cp}=\Delta\rho-(Z_1-Z_2)R_{\rm ch}^2(r)$ can be unfolded properly. The core polarization is not known experimentally; a theoretical input is therefore needed. For our purpose we will use $\Delta\rho_{\rm cp}$ as calculated in Hartree-Fock theory. In the extreme IPSM the $R_{\rm ch}^2(r)$ is due to the density $R^2(r)$ of the added proton(s) only. A complication arises by the presence of configuration admixtures in the ground state wave function. Such admixtures contribute to the charge scattering, but are not sampled by the highest multipole magnetic operator. To account for this mixing one has to use a model. We will employ a generalized valence density with mixing coefficients taken from one nucleon transfer reactions.

For the odd-even nuclei studied the most direct comparison would concern the charge density

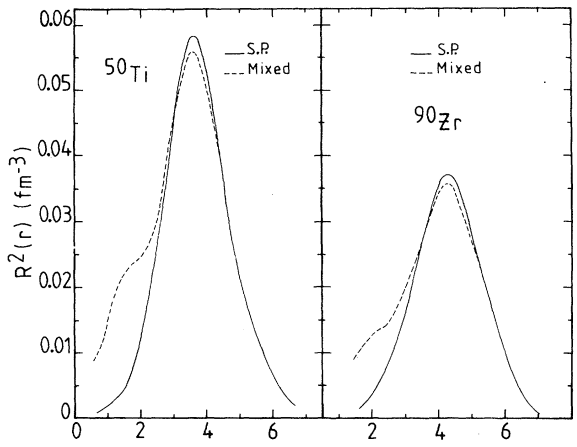

FIG. 22. Radial densities in ^{50}Ti and ^{90}Zr. The solid lines represent the single particle $f_{7/2}$ and $g_{9/2}$ configurations. The dashed line shows the mixed wave functions.

difference resulting from the addition of one proton only. However, for the nuclei considered it is difficult to obtain a model independent $\Delta\rho$ due to the presence of $J>0$ components in the charge scattering cross section. Therefore the $\Delta\rho$ of (N,Z), $(N,Z+2)$ isotone pairs with $J_0=0$ will be used.

For the $1f_{7/2}$ nuclei extensive charge scattering data exist from the Stanford experiments.[54] We have used the experimental charge densities of ^{48}Ca and ^{50}Ti and the Hartree-Fock wave functions of Decharge and Gogny[27] to calculate the core polarization $\Delta\rho_{cp}$. A two components valence nucleon density $R_{ch}^2(r)$ was taken:

$$R_{ch}^2(r)=(0.95)^2R_{1f_{7/2}}(r)+(0.3)^2R_{2p_{3/2}}(r)\ ,$$

where the mixing coefficients have been chosen to be compatible with spectroscopic factors deduced from stripping reactions.[55] Both radial wave functions were computed in a Woods-Saxon well from the best-fit geometry of ^{51}V (see Table X). The left hand part of Fig. 22 shows that $R_{ch}^2(r)$ differs in minor aspects only from the pure single particle density $R^2(r)$.

The result of the comparison between the $1f_{7/2}$ valence orbit, as determined from charge density differences, with that obtained from magnetic scattering is shown in Fig. 23. A clear discrepancy is observed: The peak of $R^2(r)$ is located at an appreciably smaller radius.

An identical analysis was performed for the $1g_{9/2}$ orbit. Here the orbital density of ^{93}Nb was compared to the charge density difference of the isotone pair ^{92}Mo-^{90}Zr. The ground state wave functions were taken to be[58] the following:

$$|\,^{90}\mathrm{Zr}\rangle=0.8\,|\,2p_{1/2}{}^2\rangle\,|\,^{88}\mathrm{Sr}\rangle +0.6\,|\,1g_{9/2}{}^2\rangle\,|\,^{88}\mathrm{Sr}\rangle\ ,$$

$$|\,^{92}\mathrm{Mo}\rangle=0.85\,|\,2p_{1/2}{}^2\rangle\,|\,1g_{5/2}{}^2\rangle\,|\,^{88}\mathrm{Sr}\rangle +0.53\,|\,1g_{9/2}{}^4\rangle\,|\,^{88}\mathrm{Sr}\rangle\ .$$

The mixed density is determined mainly by the $1g_{9/2}$ single particle configuration (see Fig. 22). Figure 24 shows that the valence density deduced

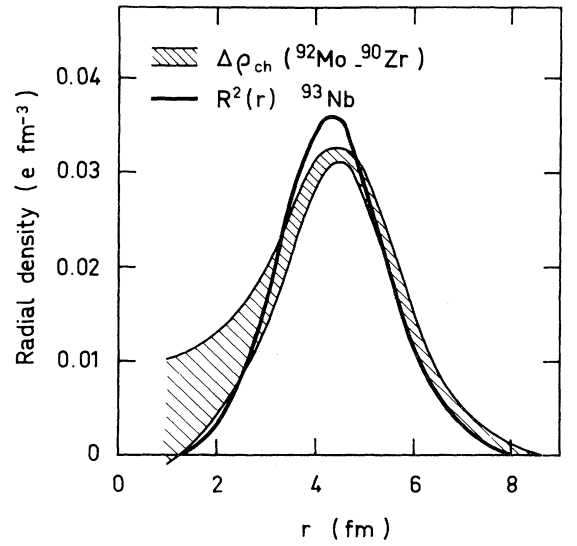

FIG. 23. Comparison between the charge density difference obtained from ^{50}Ti-^{48}Ca isotone difference and the magnetic scattering results for ^{51}V.

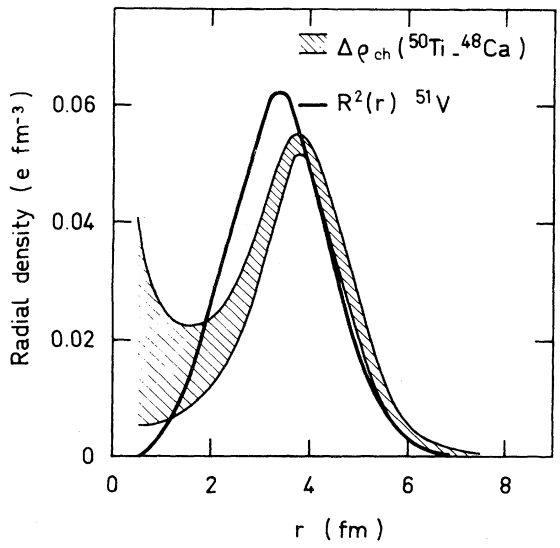

FIG. 24. Same as Fig. 23 for ^{92}Mo-^{90}Zr and ^{93}Nb.

from charge scattering extends slightly further out than $R^2(r)$ obtained via magnetic scattering. However, the disagreement is less pronounced than that observed for the $1f_{7/2}$ shell.

Several reasons can be invoked to explain the disagreement between the two quoted results. (i) The theoretical core polarization is probably not correct. It is already known that Hartree-Fock theory does not well predict experimental isotope shifts.[53,56] The larger core polarization found experimentally might be explained by taking into account quadrupole deformations and ground state correlations,[57] effects which have been neglected in the calculations cited. Indeed, in a spherical Hartree-Fock calculation the ^{48}Ca core is probably too rigid, due to neglected modes of core excitations. This would explain the better agreement for the $1g_{9/2}$ shell where the binding energy as a function of the deformation shows (Fig. 21) a deep minimum at $q=0$, a feature which is valid for ^{90}Zr as well. (ii) We have considered only two components of the charge density difference, neglecting the smaller admixtures in the ground state wave function. Although it seems reasonable, it is very difficult to determine exactly the uncertainty introduced by this assumption. (iii) For practical reasons we have considered slightly different isotone pairs from those which would be the most appropriate ones. The additional effects introduced, such as an A dependence and a residual core polarization, are difficult to estimate.

On the basis of the above analysis it appears that many model assumptions are needed to extract the valence wave functions from the charge difference between isotone pairs. We conclude that such a method cannot yield a result of accuracy comparable to that of elastic magnetic scattering.

B. Comparison with measurements of total neutron densities

Total neutron densities are traditionally determined by scattering of p, α, π, etc. While experimental data are quite accurate and complete, the extracted densities are still subject to considerable doubt. For the interpretation, assumptions concerning the reaction mechanism have to be made. The use of high-energy approximations [Glauber, Kerman, McManus, Thaler (KMT)], the use of folding models, or the neglect of higher-order processes may cause problems at the level of a few percent in the rms radius for instance. The consequence of these ambiguities is a large spread in the results obtained from different experiments or probes.

Uncertainties of several percent are of considerable importance in the discussion of neutron rms radii. Hartree-Fock theory predicts rather small differences between proton and neutron rms radii; for ^{48}Ca, a nucleus where this difference is particularly large, it amounts to only $\sim 5\%$. Modern Hartree-Fock calculations yield differences between 0.14 and 0.23 fm. An experimental precision of the order of one percent is needed to make a meaningful verification of the prediction. Using electron scattering to check the above mentioned $\rho_n(r)$ determinations thus would be very valuable.

At first sight such a check seems difficult: While hadron scattering measures total neutron densities, magnetic electron scattering measures valence nucleon densities. Looking at hadron scattering closely, however, reveals that in no reaction $\rho_n(r)$ (or $r_{\rm rms}$) is measured the way $\rho_p(r)$ is measured by (charge) electron scattering. Hadrons are strongly absorbed in the nuclear interior, with the consequence that the information obtained is limited to the low-density region. For 1 GeV proton scattering, this region starts at radii r where $\rho(r) < 0.5\ \rho(0)$, while for α, π the extreme nuclear surface radii r where $\rho(r) < 0.1\ \rho(0)$ is studied.

In this region the total density is expected to be dominated by the valence shell. This is particularly true for ^{48}Ca, where the $f_{7/2}$ shell is filled and has the highest l (is the most surface peaked). This same valence shell is studied by magnetic electron scattering for the example given in the neighboring nucleus ^{49}Ti. A direct comparison of electron and hadron scattering based on the quantity really measured by hadron scattering—the density in the tail of the nuclear distribution— should therefore be possible.

For ^{48}Ca this comparison has been performed as follows: In order to go from $\rho_n(r)$ to the valence shell density, we have used the DDHF calculation of Ref. 44. The ratio of $f_{7/2}$ to total neutron density, which in the tail region varies from 0.5 to 1, is shown in the lower part of Fig. 25. This ratio is expected to depend little on the theory employed, provided the calculated separation energies are reasonable. In order to evaluate the uncertainty in this ratio, we have used a second HF calculation[27] as well as a density calculated from a Saxon-Woods potential having identical geometry for all shells. The resulting ratios differ by less than 10%. Using this ratio and the neutron density determined from 1 GeV proton scattering by the very careful analysis

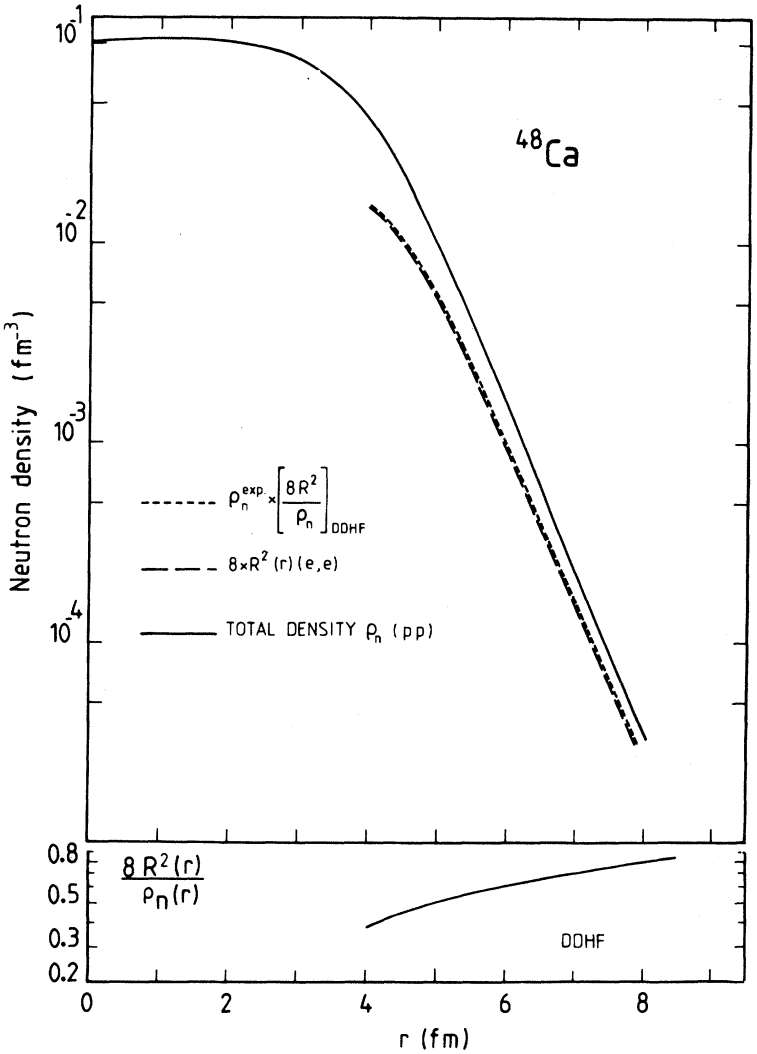

FIG. 25. Total neutron density of ^{48}Ca obtained from 1 GeV (p,p) experiment (Ref. 59) (solid line). The contribution of the $f_{7/2}$ neutrons (dashed line) is compared to the results of the present experiment for ^{49}Ti (dotted) corrected for MEC and for A dependence.

of Chaumeaux and Schaeffer[52,59] yields the $f_{7/2}$ density contribution shown in Fig. 25.

For electron scattering we start from the ^{49}Ti $f_{7/2}$ neutron radial wave function calculated in c.m. coordinates and fitted to electron scattering data. This wave function is folded with finite nucleon size and corrected for MEC in order to properly compare to the densities of Ref. 59. Given the fact that the $f_{7/2}$ neutron radii as determined by sub-Coulomb stripping reactions[60] do vary as $A^{1/3}$ from ^{40}Ca to ^{48}Ca, a 0.6% compression in the radial scale is performed when going from ^{49}Ti to ^{48}Ca. The resulting $f_{7/2}$ density for the eight neutrons in ^{48}Ca is shown in Fig. 25.

From Fig. 25 we deduce that electron scattering and the proton scattering results[52,59] perfectly agree over the entire tail region. The remaining differences in the $f_{7/2}$ density would correspond to $<0.5\%$ differences in rms valence radii. Given the uncertainties in the comparison procedure, the agreement is significant on the $\sim 1\%$ level.

While we find that electron scattering agrees with the 1 GeV (p,p) experiment of Ref. 52, this is not the case for many of the $\rho_n(r)$ determinations in the literature.[61–67] These results can be characterized by a single number giving the difference Δ between the point rms radii of neutrons and protons in ^{48}Ca. This number is found to vary from 0.04 to 0.31 fm in the different experiments available. For the high energy proton scattering results published[52,61,62] it

varies from 0.16 to 0.23 fm. This difference comes mainly from the assumptions made in the analysis, and is hardly due to the different data used. The treatment of the reactions mechanism, two-body correlations, the nucleon form factor, and spin-orbit contributions are mainly responsible for the difference. As a comparison the DDHFB calculation of Dechargé and Gogny[39] yields $\Delta=0.14$, and Ref. 59 gives 0.09 fm.

C. Coulomb energy differences

Historically, the field of Coulomb displacement energies has been linked quite closely to the one of valence nucleon wave functions. From the binding energy difference between mirror nuclei actually some of the first determinations of the nuclear size were obtained.[68] Since, a considerable effort has gone into the interpretation of the experimental Coulomb energy difference (CED).

The systematic analysis of Ref. 69 was performed under the assumption of charge symmetry of the nucleon-nucleon force. In this case the difference between the binding energies of isobaric analog states is essentially due to the Coulomb energy of the proton. It can be calculated if the charge distribution $\rho(r)$ and the radial wave function of the proton are known. Starting from realistic charge distributions and experimental ΔE, Nolen and Schiffer derived the $R(r)$ of the analog protons (assumed to be identical to the one of the corresponding valence neutrons). The rms radii found were systematically smaller than the ones derived from accepted wave functions, the difference being 10–20 %.

Magnetic electron scattering does not confirm these anomalously small radii of valence neutrons (or valence protons). The deviations between experiment and the best theoretical wave functions are of the order of only a few percent. We therefore conclude that the conceptually simple analysis of CED yields incorrect radii. This shows that Coulomb energy differences are not yet properly understood. However, the investigated correction terms to the interpretation of Ref. 69 turn out to be quite small, with the exception of the one due to the isospin impurity of the core[70,71]; this term does reduce the disagreement by ~30%. The precise effect of another term, the core compression contribution,[72] is yet to be calculated quantitatively.

The long standing disagreement between calculations and experiment, ~0.5 MeV for $A=40$, is not yet eliminated. Today, the emphasis thus lies less on the determination of $R(r)$; rather one searches for a quantitative understanding of CED, and an answer to the question[73] of whether this can be obtained without evoking charge-symmetry breaking. Investigations in this direction can now be carried out with a better chance for an unambiguous answer. For a few cases we now have both accurate charge densities and valence nucleon radial wave functions available.

D. Comparison with transfer reactions

One-nucleon transfer reactions have been investigated in great detail in the past. In general, the goal of such experiments has been to provide the spectroscopic factors S used to describe the microscopic structure of the state under consideration.

Transfer reactions involve composite particles that are strongly absorbed in the nuclear interior. Consequently, the information on the wave function of the transferred nucleon only concerns the region outside the nuclear surface. The quantity measured is, essentially, the asymptotic normalization of $R(r)$ multiplied with the spectroscopic factor. In order to extract spectroscopic factors—quantities representing an integral over the entire nuclear volume—model radial wave functions have to be used. The strong dependence of S on $R(r)$—typically an 8% change of S for a 1% change of the rms radii of $R(r)$—is often ignored. To a large degree the dispersion of values for S quoted in literature results from different choices for $R(r)$.

This uncertainty can be eliminated using the radi-

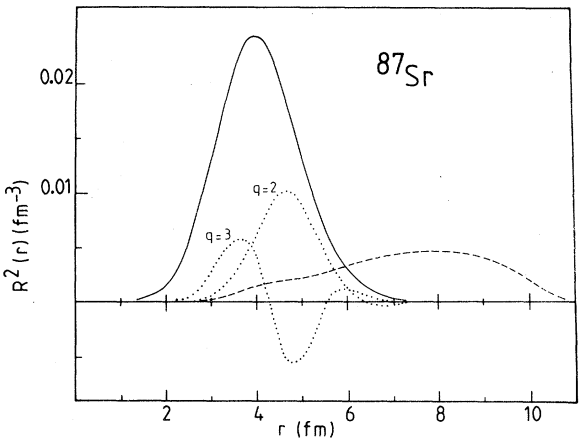

FIG. 26. Overlap of the ^{87}Sr $g_{9/2}$ radial density with the integrands of the magnetic electron scattering (dotted) or transfer reaction (dashed) experiments.

TABLE XVII. Spectroscopic factors as found in the present work and in transfer reaction experiments. Values in parenthesis are calculated using MEC-corrected radial densities.

Nucleus	Shell	α_Λ (*ee*)	α_Λ (transfer reactions)	Reference
^{49}Ti	$1f^n_{7/2}$	0.83(0.76)	1.06(0.98)	77
^{51}V	$1f^p_{7/2}$	1.01(0.93)	0.81(0.78)	78,79
^{87}Sr	$1g^n_{9/2}$	0.89(0.82)	0.63(0.56)	76
^{93}Nb	$1g^p_{9/2}$	0.93(0.86)	0.64(0.57)	80

al wave functions determined by electron scattering. This is demonstrated in Fig. 26, where we show the $R^2(r)$ of $1g_{9/2}$ neutrons in ^{87}Sr together with the integrand of Eq. (2.6) for the maximal and minimal momentum transfer of experiment. The electron scattering form factor samples $R(r)$ in the region where R is large, between 2.5 and 6 fm radius. For transfer cross sections, the quantity analogous to the integrand of Eq. (2.6) can be calculated[74,75] and is also shown in Fig. 25. This curve is calculated for a typical transfer reaction ^{87}Sr(d,p) at $E_d=25$ MeV and for a proton angle of 40°. This angle corresponds to the first maximum of the proton angular distribution, i.e., the angular region often used to extract S. (The corresponding curves for other angles are quite similar.) Figure 26 demonstrates that in spite of the relatively large energy of $E_d=25$ MeV the transfer cross section receives its largest contribution from a radial region where $R(r)$ is very small, and where its shape is essentially imposed by the falloff determined by the separation energy.

Using the $R(r)$ determined from electron scattering, one can reanalyze the transfer cross sections. This allows an absolute determination of the spectroscopic factors. Hence a good check of the occupation number sum rules that often have been used for *ad hoc* renormalization of experimental values for S becomes possible. The spectroscopic factors determined by this approach can be compared to the values of α_Λ deduced from magnetic electron scattering.

The spectroscopic factors quoted in the literature have been calculated using various (not always specified) prescriptions for the WS potential. In order to employ the information on $R(r)$ provided by magnetic scattering, one has to reanalyze the transfer data, as done, e.g., in Ref. 76 for the ^{87}Sr data. If the $R(r)$ used are reasonably close to the ones required by electron scattering, the spectroscopic factors can be corrected for the difference without complete reanalysis. This can be done by calculating with different Woods-Saxon wells the change in the asymptotic norm (the quantity transfer reactions are most sensitive to) with the change in the WS parameters.

Starting from the transfer data of Refs. 55 and 77–79 we have recalculated the spectroscopic factors to correspond to the $R(r)$ measured by magnetic scattering. This leads to changes in S up to 25%. Ground state properties can be deduced from these spectroscopic factors via two types of sum rules. From the sum over all states in the residual nucleus the number of particles or holes in a given shell can be obtained.[80] If both, particle and hole spectroscopic factors are measured, the sum-rule value $(2j+1)$ times a center of mass correction factor should be obtained. From a weighted sum[81] over pickup spectroscopic factors

$$\alpha_\Lambda=(2j+1)\sum_f(-)^{J_f+2j+\Lambda}\begin{Bmatrix} jj\Lambda \\ jjJ_f \end{Bmatrix} S_{jf}^{-}$$

and an analogous expression for stripping, the α_Λ

TABLE XVIII. Number of particles/holes as derived from transfer reactions. The sum rule values of ^{51}V and ^{87}Sr are also given.

Nucleus	Shell	Particles/holes	Particles + holes	Sum rule
^{49}Ti	$1f^n_{7/2}$	8.4(7.7) p		
^{51}V	$1f^p_{7/2}$		6.1(5.8)	8.47
^{87}Sr	$1g^n_{9/2}$		6.5(5.9)	10.61
^{93}Nb	$1g^p_{9/2}$	5.5(4.9) h		

appearing in Eq. (2.6) can be calculated. This latter sum rule heavily favors excited states in the residual nucleus of low J_f, since the "stretched" $6j$ symbol rapidly decreases with increasing J_f.

In Table XVII we compare the α_Λ as obtained from electron scattering with those deduced by the quoted sum rule from transfer reactions. In Table XVIII, we list the number of $l=3,4$ particle (holes) or their sum as derived from transfer reactions.

Several conclusions can be drawn from these tables: The α_7,α_9 derived from spectroscopic factors in general are $\sim 30\%$ lower than the ones directly determined by electron scattering. The only exception is ^{49}Ti, where both α_7 and the total number of $f_{7/2}$ neutrons (Table XVIII) exceeds the sum rule value. The ^{49}Ti spectroscopic factors of Ref. 82 would lead to a more correct $\alpha_7=0.89$ and a reasonable $1f_{7/2}$ neutron occupation number; unfortunately, these values have been calculated for a not quoted $R(r)$.

For the occupation numbers of the different shells, the nuclei where the sum of both particles and holes has been observed are most interesting. For ^{87}Sr and ^{51}V we find that the sum rule limits are exhausted to 61% and 72% only. This indicates that a considerable fraction of the $l=3$ and 4 strength has not yet been observed. This strength is probably located at higher excitation energy ($E>6$ MeV) or in the continuum. Consequently the often practiced renormalization of experimental spectroscopic factors to the sum rule value is inadequate.

As mentioned above, the sum rule for α_Λ is less sensitive to high-J states occurring at high excitation energy in the residual nucleus. This explains why the α_Λ values are closer to the naive value given by the strict single-particle model than the occupation numbers. The latter ones, even in the presence of configuration mixing, should yield the sum rule values. The large amount by which they deviate from the sum rule values is therefore not well understood.

IX. SUMMARY

In the preceding sections we have presented a detailed investigation of elastic electron scattering from the ground state magnetization distribution of ^{49}Ti, ^{51}V, ^{59}Co, ^{87}Sr, ^{93}Nb, ^{209}Bi. Particular emphasis has been placed on the measurement and interpretation of the highest multipole component which dominates the magnetic cross section at large momentum transfer. For nuclei satisfying some specific criteria—highest possible multipolarity, stretched configuration—a measurement of this multipole distribution allows a precise determination of the radial wave function of the unpaired proton or neutron.

Experimental data have been taken in the range of momentum transfer $q=1.7$ to 3.3 fm^{-1}. The main lobe of the magnetic form factor of highest multipolarity was thus well determined. The precision obtained on its q dependence is closely related to the precision on the valence wave functions deduced by fitting the data with phenomenological single-particle wave functions. The model dependence of the results has been minimized by parametrizing $R(r)$ in terms of a solution of the Schrödinger equation for a Woods-Saxon potential. Hereby many unphysical features of phenomenological $R(r)$ can be suppressed, and information from other experiments be incorporated.

The results obtained concern the radial wave functions $R(r)$ for the $f_{7/2}$ shell nuclei ^{49}Ti, ^{51}V and the $g_{9/2}$ shell nuclei ^{87}Sr and ^{93}Nb. We have shown that these $R(r)$ are well measured in the region between 2 and 6 fm, in contrast to experiments using strongly interacting probes which are sensitive to $R(r)$ at large radii only. The present experiments thus provide for the first time a precise measurement of $R(r)$ in the region where $R(r)$ is large and where the dominating part of the integral strength is located. We have shown that the rms radii derived from these radial wave functions are accurate to 1%.

For ^{49}Ti and ^{87}Sr our results concern $1f_{7/2}$ and $1g_{9/2}$ neutron radial wave functions. It was shown that by magnetic electron scattering neutron radial wave functions can be determined as well as the radial wave functions for protons. From the data, the difference between neutron and proton radial wave functions—a quantity of particular interest—can be obtained directly, and in a largely model independent way.

Various corrections due to configuration mixing and the meson exchange current have been investigated. Using the existing calculations[33] we found that the core polarization effect has a negligible influence on the shape of the $M\Lambda$ form factor, modifying the rms radius of the corresponding orbitals by $\sim 0.3\%$. Only the lower multipoles are strongly quenched and modified in shape, in a manner that depends on the residual force involved. For a quantitative understanding of the core polarization effect on these lower multipoles, a residual interaction derived in a self-consistent way (i.e., with the same

phenomenological force as the central field) would be needed.

A detailed investigation of the effect of MEC also has been performed. We show that use of the appropriate $R(r)$ in the MEC calculation and the inclusion of the πNN vertex form factor leads to a smaller effect on the rms radius than previoulsy quoted. We actually found a change due to the exchange currents of the extracted rms radii which amounts to 1%. New results[37] show that the sign of the nuclear isobar current, which becomes increasingly important at large q, had been calculated incorrectly; the correct sign will reduce the MEC correction to a negligible amount for the $M\Lambda$ form factors considered.

Our results have been compared to predictions from three different mean field calculations, both in q space and in configuration space. As a general feature we observe that all theories predict too rapid a falloff for the highest multipole form factors. This corresponds to too large a radial extension for the theoretical radial wave functions. The best agreement is obtained for the DDHFB calculation, which differs by 2% and 1.5% from the experimental results for the rms valence radii of the $f_{7/2}$ and $g_{9/2}$ orbits, respectively.

The experimental ratio of neutron to proton radii is 1.3% smaller than that given by the DDHFB calculation. The same calculation also gives a fairly good agreement for the separation energies of nuclei studied. The consistency of these results can probably be assigned to the choice of the phenomenological force and to the self-consistent treatment of the pairing correlations.

A complementary effect which might explain the difference between Hartree-Fock theories and experimental data has been suggested recently by Lejeune.[83] A study of the single particle properties of a nucleus in a dynamic mean field yields rms radii that, compared to a static calculation, are decreased by about 1% for ^{49}Ti and ^{51}V and by 0.2% for ^{93}Nb.

Our $f_{7/2}$ neutron radial wave function has been compared to a recent careful analysis of 1 GeV proton scattering data. We found that a value for $r_n - r_p$ of 0.09 fm for ^{48}Ca, as found in this analysis, is consistent with our electron scattering measurements.

The accurate determination of $R(r)$ has considerable impact on the interpretation of the spectroscopic factors S used so extensively in nuclear physics. The calculation of spectroscopic factors from transfer reaction data needs a very model dependent extrapolation from the quantity measured—the asymptotic norm of $R(r)$—to the integral over all radii, i.e., the spectroscopic factors. Knowing $R(r)$ from magnetic electron scattering allows us to obtain absolute spectroscopic factors, and to check the sum rules often utilized to normalize S. We have analyzed both occupation number sum rules and the highest multipole moment sum rules. For the nuclei investigated, we find that transfer reactions on the average locate only 70% of the strength expected. This makes the often practiced normalization of spectroscopic factors to sum rule values rather doubtful. We deduce that transfer reactions miss about 30% of the total strength, which is likely to be found at excitation energies of >6 MeV, or in the continuum.

ACKNOWLEDGMENTS

We would like to thank D. Gogny for many illuminating discussions, calculations, and constant theoretical advice. We express our gratitude to C. Tzara for his continuous support and fruitful remarks. We are indebted to K. Arita, X. Campi, J. Dechargé, A. E. L. Dieperink, J. Dubach, M. Girod, J. W. Negele, and T. Suzuki for providing us with theoretical results before publication. We also thank A. Nakada and H. DeVries for their collaboration during the initial phase of the magnetic scattering experiments. This work was supported in part by the Foundation for Fundamental Research on Matter (FOM), Netherlands Organization for the Advancement of Pure Research (ZWO), and the Swiss National Science Foundation.

[1]T. W. Donnelly and J. D. Walecka, Nucl. Phys. A201, 81 (1973).

[2]C. de Jager, C. DeVries, and H. DeVries, Nucl. Data Tables 14, 479 (1974).

[3]G. C. Li, I. Sick, J. D. Walecka, and G. E. Walker, Phys. Lett. 32B, 317 (1970).

[4]P. de Witt Huberts, J. B. Bellicard, B. Frois, M. Huet, P. Leconte, A. Nakada, X-H. Phan, S. Turck, L. Lapikás, H. DeVries, and I. Sick, Phys. Lett. 60B, 157 (1976).

[5]I. Sick, J. B. Bellicard, J. M. Cavedon, B. Frois, M. Huet, P. Leconte, A. Nakada, X-H. Phan, S. Platchkov, P. de Witt Huberts, and L. Lapikás, Phys. Rev. Lett. 38, 1259 (1977).

[6]P. de Witt Huberts, L. Lapikás, H. DeVries, J. B. Belli-

card, J. M. Cavedon, B. Frois, M. Huet, P. Leconte, A. Nakada, X-H. Phan, S. K. Platchkov, and I. Sick, Phys. Lett. 71B, 317 (1977).

[7]S. Platchkov, J. B. Bellicard, J. M. Cavedon, B. Frois, D. Goutte, M. Huet, P. Leconte, X-H. Phan, I. Sick, P. de Witt Huberts, and L. Lapikás, Phys. Lett. 86B, 1 (1979).

[8]P. Leconte, J. Mougey, A. Tomasso, P. Barreau, J. B. Bellicard, M. Bernheim, A. Bussière de Nercy, L. Cohen, J. C. Comoretto, J. Dupont, S. Frullani, C. Grunberg, J. M. Hisleur, J. Le Devehat, M. Lefevre, G. Lemarchand, J. Millaud, D. Royer, and R. Salvaudon, Nucl. Instrum. Methods 169, 401 (1980).

[9]P. Leconte, thesis, University of Paris, 1976 (unpublished).

[10]C. Cohen, C. Grunberg, and J. Le Devehat, Nucl. Instrum. Methods 103, 125 (1972).

[11]J. Millaud, thesis, University of Paris, 1975 (unpublished).

[12]L. W. Mo and Y. S. Tsai, Rev. Mod. Phys. 41, 205 (1969).

[13]H. Crannel, Phys. Rev. 148, 1107 (1966).

[14]I. Sick and J. McCarthy, Nucl. Phys. A150, 631 (1970).

[15]I. Sick, Nucl. Phys. A208, 557 (1973).

[16]I. Sick, Nucl. Phys. A218, 509 (1974).

[17]B. Frois, J. B. Bellicard, J. M. Cavedon, M. Huet, A. Nakada, P. Leconte, X-H. Phan, and I. Sick, Phys. Rev. Lett. 38, 151 (1977).

[18]K. Arita, A. Enomoto, S. Oguro, Y. Mizumo, T. Nakazato, S. Ohsawa, T. Saito, T. Terasawa, and Y. Torizuka, Phys. Rev. C 23, 1483 (1981).

[19]J. R. Moreira, I. C. Nascimento, K. Arita, J. Friedrich, A. Enomoto, T. Terasawa, and Y. Torizuka, Phys. Rev. Lett. 36, 566 (1976).

[20]R. C. York and G. A. Peterson, Phys. Rev. C 19, 574 (1979).

[21]L. R. B. Elton and A. Swift, Nucl. Phys. A94, 52 (1967).

[22]C. M. Perey and F. G. Perey, At. Data Nucl. Data Tables 13, 293 (1974).

[23]F. Borkowski, P. Peuser, G. G. Simon, V. H. Walther, and R. D. Wendling, Nucl. Phys. A222, 269 (1974).

[24]S. Gartenhaus and C. Schwartz, Phys. Rev. 108, 482 (1957).

[25]L. J. Tassie and F. C. Barker, Phys. Rev. 111, 940 (1958).

[26]L. Lapikás, in *Proceedings of the International Conference on Nuclear Physics with Electromagnetic Interactions, Mainz, 1979,* edited by H. Arenhövel and D. Drechsel (Springer, Berlin, 1979), p. 41; L. Lapikás, in *Proceedings of the Conference on Modern Trends in Elastic Electron Scattering, Amsterdam, 1978,* edited by C. DeVries (Instituut voor Kernphysisch Onderzoek, Amsterdam, 1978), p. 49.

[27]J. Dechargé and D. Gogny, private communication.

[28]K. Arita, in *Proceedings of the International Conference on Nuclear Structure, Tokyo, 1977,* edited by T. Marumori (Physical Society of Japan, Tokyo, 1978), p. 252, and private communication.

[29]E. Moya de Guerra and A. E. L. Dieperink, Phys. Rev. C 18, 1596 (1978).

[30]T. W. Donnelly and A. Gokalp, Nucl. Phys. A353, 403 (1981).

[31]A. E. L. Dieperink, private communication.

[32]J. Dubach, J. H. Koch, and T. W. Donnelly, Nucl. Phys. A271, 279 (1976).

[33]T. Suzuki, H. Hyuga, and A. Arima, Z. Phys. A 293, 5 (1979); T. Suzuki, Ph.D. thesis, University of Tokyo, 1978 (unpublished).

[34]J. Dubach, Phys. Lett. 81B, 124 (1979); Nucl. Phys. A340, 271 (1980).

[35]K. Erkelenz, Phys. Rep. 13C, 208 (1974).

[36]J. A. Lock and L. L. Foldy, Ann. Phys. (N.Y.) 93, 276 (1974).

[37]J. F. Mathiot and B. Desplanques, Phys. Lett. 101B, 141 (1981).

[38]K. A. Brueckner, Phys. Rev. 96, 508 (1954); 97, 1344 (1955).

[39]J. Dechargé and D. Gogny, Phys. Rev. C 21, 1568 (1980).

[40]P. Quentin and H. Flocard, Annu. Rev. Nucl. Part. Sci. 28, 527 (1978).

[41]J. P. Svenne, Adv. Nucl. Phys. 11, 179 (1979).

[42]A. L. Goodman, Adv. Nucl. Phys. 11, 263 (1979).

[43]J. W. Negele, Phys. Rev. C 1, 1260 (1970).

[44]X. Campi and D. W. Sprung, Nucl. Phys. A194, 401 (1972); X. Campi, private communication.

[45]D. W. Sprung and P. K. Banerjee, Nucl. Phys. A168, 273 (1971).

[46]J. W. Negele and D. Vautherin, Phys. Rev. C 5, 1472 (1972); J. W. Negele, private communication.

[47]D. Gogny, in *Nuclear Self-consistent Fields;* Proceedings of the International Conference held at the International Center for Theoretical Physics, Trieste, Italy, 1975, edited by G. Ripka and M. Porneuf (North-Holland, Amsterdam, 1975), p. 333.

[48]H. DeVries, thesis, University of Amsterdam, 1973 (unpublished).

[49]G. Box, thesis, University of Amsterdam, 1976 (unpublished).

[50]H. D. Wohlfahrt, E. B. Shere, M. V. Hoehn, Y. Yamazaki, and R. M. Steffen, Phys. Rev. C 23, 533 (1981).

[51]M. Girod and D. Gogny, private communication.

[52]A. Chaumeaux, V. Layly, and R. Schaeffer, Ann. Phys. (N.Y.) 116, 247 (1978).

[53]J. W. Negele and G. A. Rinker, Phys. Rev. C 15, 1499 (1977).

[54]R. F. Frosch, R. Hofstadter, J. S. McCarthy, G. K. Noldeke, K. J. Van Oostrum, M. R. Yearian, B. C. Clark, R. Herman, and D. G. Ravenhall, Phys. Rev. 174, 1380 (1968); J. Heisenberg, R. Hofstadter, J. McCarthy, R. Herman, B. Clark, and D. G. Ravenhall, Phys. Rev. C 6, 381 (1972).

[55]E. Newman and J. C. Hiebert, Nucl. Phys. 110, 366 (1968).

[56]H. D. Wohlfart, in *Proceedings of the International*

Conference on Nuclear Physics with Electromagnetic Interactions, Mainz, 1979, edited by H. Arenhövel and D. Drechsel (Springer, Berlin, 1979), p. 65.

[57]P. G. Reinhard and D. Drechsel, Z. Phys. A 290, 85 (1979).

[58]B. Dreher, Ph.D. thesis, University of Mainz, 1974 (unpublished).

[59]A. Chaumeaux and R. Schaeffer, private communication.

[60]J. L. Durell, C. A. Harter, J. N. Mo, and W. R. Phillips, Nucl. Phys. A334, 144 (1980).

[61]L. Ray, Phys. Rev. C 19, 1855 (1979).

[62]G. D. Alkhazov, T. Bauer, R. Beurtey, A. Boudard, G. Bruge, A. Chaumeaux, P. Couvert, G. Cvijanovich, H. H. Duhm, J. M. Fontaine, D. Garreta, A. V. Kulikov, D. Legrand, J. C. Lugol, J. Saudinos, J. Thirion, and A. A. Vorobyov, Nucl. Phys. A274, 443 (1976).

[63]G. K. Varma and L. Zamick, Phys. Rev. C 16, 308 (1977).

[64]G. M. Lerner, J. C. Hiebert, L. L. Rutledge Jr., C. Papanicolas, and A. M. Bernstein, Phys. Rev. C 12, 145 (1975).

[65]I. Brissaud, Y. Le Bornec, B. Tatischeff, L. Bimbot, M. K. Brussel, and G. Duhamel, Nucl. Phys. A191, 145 (1972); G. D. Alkhazov *et al., ibid.* A280, 365 (1977).

[66]H. J. Gils, in *Proceedings of the Karlsruhe International Discussion Meeting, "What Do We Know About the Radial Shape of Nuclei in the Ca region?,* edited by H. Rebel, H. J. Grils, and G. Schatz (Institute für Angewandte Kernphysik, Karlsruhe, 1979).

[67]M. J. Jacobson, G. R. Burleson, J. R. Calarco, M. D. Cooper, D. C. Hagerman, I. Halpern, R. H. Jeppeson, K. F. Johnson, L. D. Knutson, R. E. Marrs, H. O. Meyer, and R. P. Redwine, Phys. Rev. Lett. 38, 1201 (1977).

[68]H. Bethe, Phys. Rev. 54, 436 (1938).

[69]J. Nolen and J. Schiffer, Annu. Rev. Nucl. Sci. 19, 471 (1969).

[70]E. H. Auerbach, S. Kahana, and J. Weneser, Phys. Rev. Lett. 23, 1253 (1969).

[71]N. V. Giai, D. Vautherin, M. Veneroni, and D. M. Brink, Phys. Lett. 35B, 135 (1971).

[72]S. Shlomo, Rep. Prog. Phys. 41, 957 (1978).

[73]J. W. Negele, in *Proceedings of the International Conference on Nuclear Structure and Spectroscopy, Amsterdam, 1974,* edited by H. P. Blok and A. E. L. Dieperink (Scholars Press, Amsterdam, 1974), p. 618.

[74]I. Sick, Comm. Nucl. Part. Phys. 9, 55 (1980).

[75]F. Rösel, private communication.

[76]A. Moalem and E. Friedman, Phys. Rev. Lett. 40, 1064 (1978).

[77]A. Jamshidi and W. P. Alford, Phys. Rev. C 8, 1796 (1973).

[78]M. Matoba, Nucl. Phys. 118, 207 (1968).

[79]M. R. Cates, J. B. Ball, and E. Newman, Phys. Rev. 187, 1682 (1969).

[80]J. B. French, Phys. Lett. 15, 327 (1965).

[81]C. F. Clement, Nucl. Phys. 213, 469 (1973).

[82]P. Wilhjem, O. Hausen, J. R. Comfort, C. K. Bockelman, P. D. Barnes, and A. Sperduto, Phys. Rev. 166, 1121 (1968).

[83]A. Lejeune, Nucl. Phys. A339, 317 (1980).

[84]M. V. Hynes, H. Miska, B. Norum, W. Bertozzi, S. Kowalski, F. N. Rad, C. P. Sargent, T. Sasanuma, W. Turchinetz, and B. L. Berman, Phys. Rev. Lett. 42, 1444 (1979).